**Universidade de Aveiro**
**Ano 2019**

Departamento de Engenharia de Materiais e Cerâmica

**Rodrigo Miguel Franco dos Santos**

# Electrodos de (Ni,Mo)-$TiO_2$ para pilhas de combustiveis de óxido sólido reversiveis.

# (Ni,Mo)-$TiO_2$ electrodes for electrochemical applications.

**Universidade de Aveiro**
**Ano 2019**

Departamento de Engenharia de Materiais e Cerâmica

**Rodrigo Miguel Franco dos Santos**

# Electrodos de (Ni,Mo)-$TiO_2$ para pilhas de combustiveis de óxido sólido reversiveis.

# (Ni,Mo)-$TiO_2$ electrodes for electrochemical applications.

Dissertação apresentada à Universidade de Aveiro para cumprimento dos requisitos necessários à obtenção do grau de Mestre em Engenharia de Materiais, realizada sob a orientação científica do Doutor Jorge Ribeiro Frade, Professor Catedrático do Departamento de Engenharia de Materiais da Universidade de Aveiro, e do Doutor Andrei Kavaleuski, Investigador Principal do Departamento de Engenharia de Materiais da Universidade de Aveiro.

**o júri**

| | |
|---|---|
| Presidente | Prof. Doutor Fernando Manuel Bico Marques<br>Professor Catedrático do Departamento de Engenharia de Materiais e Cerâmica da Universidade de Aveiro |
| Vogal – Arguente Principal | Doutor Aliaksandr Shaula<br>Investigador Principal do Departamento de Engenharia Mecânica da Universidade de Aveiro |
| Vogal – Orientador | Prof. Doutor Jorge Ribeiro Frade<br>Professor Catedrático do Departamento de Engenharia de Materiais e Cerâmica da Universidade de Aveiro |

**agradecimentos**

Á minha família e amigos, em especial aos meus pais, pelo apoio e preocupação sempre me demonstrado.
Ao Doutor Jorge Frade e ao Doutor Andrei Kavaleuski, pelo conhecimento partilhado e pela disponibilidade para o esclarecimento de dúvidas.
A todos os meus colegas de laboratório que sempre estiveram disponíveis para me auxiliarem em qualquer questão, em especial ao Kiryl Zakharchuk e a Daniela Lopes pela paciência, sempre me demonstrada.
Aos técnicos do departamento de Engenharia de Materiais e Cerâmica da Universidade de Aveiro, que possibilitaram a recolha dos dados em especial ao Artur Sarabando e à Marta Ferro.
Finalmente, à Universidade de Aveiro, pela bolsa do projeto HEALING – (POCI-01-0145-FEDER-032036 e 32036-02/SAICT/2017), que disponibilizou os meios necessário para a realização deste trabalho.

**palavras-chave** Propriedades eletroquímicas; Materiais cerâmicos; Fases de Magnéli; Liga de Ni-Mo; SOFC, Eletrólise

**resumo**

Um dos maiores problemas das energias renováveis é a sua dependência das condições climatéricas. Caso estas sejam favoráveis, será produzido excesso de energia sendo esta desperdiçada devido à baixa capacidade de armazenamento por parte da tecnologia disponível. Caso contrário, se as condições climatéricas forem adversas, a energia produzida será insuficiente, sendo necessário recorrer ao consumo dos combustíveis fosseis para assegurar uma produção constante de eletricidade.

As pilhas de combustível de oxido sólido reversíveis (PCOSR) podem contribuir para a resolução deste problema, devido a sua capacidade de operar em dois modos diferentes, nos quais o hidrogénio ou o carbono atuam como unidades para o armazenamento de energia. Num dos modos, a eletricidade é produzida pela transformação do hidrogénio em água, este deverá ser utilizado aquando as condições climatéricas forem adversas. No outro, o hidrogénio é produzido através da água através da utilização do excesso elétrico produzido pelas energias renovais, aquando as condições forem favoráveis. Apesar de ser relativamente eficiente e muito promissor, esta tecnologia não se encontra amplamente disponível, devido à elevada degradação dos elétrodos, dos materiais catalíticos serem dispendiosos, baixa resistência à deposição de carvão e dificuldades no armazenamento do hidrogénio, entre outros.

Inicialmente, este trabalho foi focado no desenvolvimento de um material compósito para ser aplicado como elétrodo de combustível em Pilhas de Combustível de Óxido Sólido Reversíveis (PCOSR). Baseado na revisão bibliográfica, os NiTiO3 (referência), NiTiO3 (90% mol.) – MoO3 (10 % mol.) e NiTiO3 (80% mol.) – MoO3 (20% mol.) compósitos foram selecionados, preparados e caracterizados em condições conformes à da operação das PCOSR. As medidas elétricas assim como os estudos estruturais revelaram uma rápida degradação devido à oxidação, mesmo a baixa temperatura, evidenciando que a sua aplicação nas PCOSR será problemática. Adicionalmente, os materiais preparados foram avaliados como electro catalisadores para a eletrolise de água alcalina, sendo demonstrado a sua potencial aplicabilidade para favorecer o processo de evolução do hidrogénio, aquando a polarização catódica aplicada for suficiente para prevenir a oxidação das fases de Magnéli assim como a decomposição da fase metálica, ou ciclos de redox poderão ser aplicados para recuperar a superfície dos elétrodos. Os dados obtidos experimentalmente foram relacionados com predições termodinâmicas pelo cálculo de diagramas de Ellingham e Pourbaix.

**keywords** Electrochemical properties; Ceramic materials; Magnéli phases; Ni-Mo alloy; SOFC; Electrolysis;

**abstract**

One of the major issues of the renewable energies is their dependence of the weather conditions. If those are favourable, the energy will be produced in excess and wasted, due to limited capacity of the existing storage technologies. On the contrary, if the weather conditions are unfavourable, the energy produced will be insufficient, thus requiring the consumption of fossils fuels to assure a constant electrical output.

The reversible solid oxide fuel cells (RSOFC) can contribute to the solution of this problem, provided by capability to operate in two different modes, with the hydrogen or carbon as the energy carrier. In one mode, the electricity is produced by the transformation of hydrogen into water, this is to be used when the weather conditions are unfavourable. In reverse operation mode, hydrogen is produced from the water using the excess of electricity produced by renewable energies, when the conditions are favourable. Although being fairly efficient and highly promising, this technology is still not widely available due to high electrode degradation, expensive catalytic materials, low resistance to carbon deposition and difficulties of the hydrogen storage, among others.

This work was initially focusing on development of a composite material for fuel electrodes of Reversible Solid Oxide Fuel Cells (RSOFC). Base on the literature review, the nominal $NiTiO_3$ (reference), $NiTiO_3$ (90% mol.)- $MoO_3$ (10% mol.) and $NiTiO_3$ (80% mol.)- $MoO_3$ (20% mol.) compositions were selected, prepared and characterized in the conditions, relevant for RSOFC operation. The electrical measurements combined with structural studies revealed fast degradation due to oxidation even at low temperatures, rendering their application problematic for RSOFC technology. Additional assessment of the prepared materials as electrocatalysts for alkaline water electrolysis was performed and demonstrated their potential applicability for boosting hydrogen evolution process if the applied cathodic polarization is sufficient to prevent oxidation of the Magnéli phases and decomposition of metallic phases, or redox cycling can be applied to recover the electrode surface. The obtained experimental results were correlated with thermodynamic predictions made by calculation of Ellingham and Pourbaix diagrams.

# Index

# List of Figures

# List of Tables

# List of Abbreviations

| | *Name* | *Units* |
|---|---|---|
| *AWE* | Alkaline Water Electrolysis | |
| *SOEC* | Solid Oxide Electrolysis Cell | |
| *PEME* | Polymer-Electrolyte Membrane Electrolyser | |
| $\Delta_G$ | Gibbs free energy | |
| *AFC* | Alkaline Fuel Cell | |
| *PAFC* | Phosphoric Acid Fuel Cell | |
| *MCFC* | Molten Carbonate Fuel Cell | |
| *SOFC* | Solid Oxide Fuel Cell | |
| *PEMFC* | Proton Exchange Membrane Fuel Cell | |
| *RSOFC* | Reversible Solid Oxide Fuel Cell | |
| $\Delta l/l_0$ | Length change | % |
| $R$ | Ideal Gas Constant | $J.K^{-1}.mol^{-1}$ |
| $T$ | Temperature | K |
| $pO_2$ | Oxygen pressure | atm |
| $\frac{pH_2O}{pH_2}$ | Ratio of oxidized to reduce species of hydrogen | % |
| $\eta_a$ | Anodic polarization | V |
| $\eta_c$ | Cathodic polarization | V |
| $F$ | Faraday constant | C/mol |
| $\frac{pCO_2}{pCO}$ | Ratio of oxidized to reduce species of carbon | % |
| $R_T$ | Total resistance | Ω |
| $R_{Sample}$ | Sample resistance | Ω |
| $R_W$ | Wire resistance | Ω |
| $R_C$ | Contacts resistance | Ω |
| $wt_1$ | Dry mass | g |
| $wt_2$ | Wet mass | g |
| $wt_3$ | Apparent mass | g |

# 1 Introduction

The energetic consumption nowadays is increasing, thus requiring electricity production with the lowest environmental impact as possible, like renewable energies. However, their production is intermitted due to the dependence on the weather conditions. So, if these are favourable, the energy is produced in excess, while in opposite case the energy produced is lower than the required. The actual technology for energy storage, on larger scales, currently is not competitive with the fuel fossils. The excess of electricity produced by renewable sources is mostly wasted, and the fossil fuels are used to produce the corresponding energy, to assure an electrical output constant.

With an alliance between an efficient storage technology with renewable energies, the use of fuel fossils for electricity production is expected to decrease drastically. Therefore, it is imperative to develop efficient technologies to store electricity at larger scales.

## 1.1 Hydrogen as an energy carrier.

Hydrogen can be produced from water by an electrochemical reaction, the water electrolysis, in which electrical energy is transformed into chemical energy, as during a battery charge. Reversing the water electrolysis reaction allows to transform the chemical energy stored in $H_2$ into electricity with simultaneous formation of water as by-product. Using these reactions, the $H_2$ can store the excess of electricity produced from renewable sources, to be then used when required. For that two electrochemical devices are required, the first one, to store energy by the $H_2$ production, an electrolyser cell, and another to convert into electricity, a fuel cell [1].

### 1.1.1 Electrolyser Cell.

An electrolyser cell transforms $H_2O$ into $H_2$, by the water electrolysis reaction. The cell includes two electrodes, cathode and anode, where the electrochemical reactions proceeds, separated by an electrolyte that carries ionic species between electrodes. On the cathode, the hydrogen from $H_2O$ is reduced to $H_2$, with the release of ionic species, such as hydroxides ($OH^-$) or oxygen ions ($O^{-2}$) in the case of the Alkaline Water Electrolysis (AWE) and Solid Oxide Electrolysis Cell (SOEC), correspondingly. These species migrate through the electrolyte towards the anode, where oxidation to molecular oxygen ($O_2$) takes place. In the case of Polymer-Electrolyte Membrane Electrolyser (PEME), the $H_2O$ discharges at the anode where oxygen is oxidized to $O_2$. This process is accompanied by a release of hydrogen ions ($H^+$) to the electrolyte, that will migrate to the cathode to be reduced to $H_2$ [2]. The described electrochemical reactions take place when electrical current is applied.

In 2015 around 50 Mt of $H_2$ were produced, but only 4% of those was by water electrolysis. This process is highly expensive due to high cost of materials with good electrocatalytic activity. In addition, it results in a high electrical consumption when compared with the conventional methods:

steam reforming of hydrocarbons or coal gasification [3]. Thus, this technology requires further improvements to compete with those based on fossil fuels.

The technologies that use water electrolysis to produce $H_2$ can be divided by their operating temperature. The alkaline or acidic electrolysis and polymer-electrolyte membrane electrolyser (PEME) are low-temperature electrolysers, while the solid oxide electrolyser cell (SOEC) is a high-temperature electrolyser [4]. The operating temperature depends on the required temperature, at which the electrolyte acts as an ionic conductor. In the alkaline or acidic electrolysis, the electrolyte is a solution, in which the ionic conduction can proceed at lower temperature like 60 to 80 °C [5]. In the cases of PEME and SOEC, the electrolyte is solid. In PEME, the electrolyte is a proton exchange membrane allowing the proton conduction at 50-80 °C [5], whereas for the SOEC the electrolyte is a solid oxide requiring a higher temperature for the ionic conduction to proceed, like 600 to 800 °C [4].

The efficiency of the water electrolysis is affected by the operating temperature, namely, it increases on heating owing to the endothermic effect of the reaction. Figure 1.1 is a representation of the thermodynamics of the water electrolysis, showing that the required electric energy ($\Delta G$) for the electrolyses decreases with the increase of operation temperature [4].

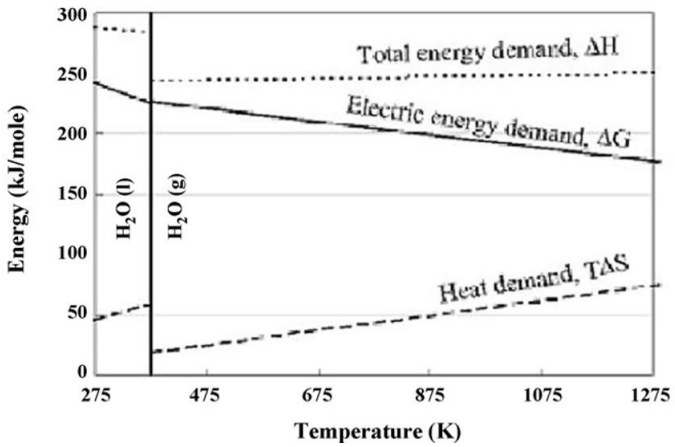


*Figure 1.1. Dependence of the water electrolysis thermodynamics with the temperature as the required electric energy necessary to apply to carry on [4].*

### 1.1.2 Fuel cell.

Fuel cells are devices that produce electricity and heat due to electrochemical reactions, the reverse of the water electrolysis. The range of power produced in various applications may reach up to 1 to 10 MW [6]. Thus, these devices can be applied in different situations from personal devices like computers or cars to power generation stations.

The fuel cell structure is similar to an electrolyser cell, in which the difference is the reactions that happen on each electrode. At the anode, the hydrogen oxidizes to form $H_2O$. At the

cathode, $O_2$ is reduced to $O^{2-}$, that migrates through the electrolyte towards the anode and completes the electrical circuit.

The fuel cell devices are classified depending on their electrolyte type. The Alkaline Fuel Cell (AFC) and Phosphoric Acid Fuel Cell (PAFC) are the ones in which the electrolyte is a solution, while the solid ones are Molten Carbonate Fuel Cell (MCFC); Solid Oxide Fuel Cell (SOFC) and Proton Exchange Membrane Fuel Cell (PEMFC) [6].

The figure 1.2 shows that the fuel cells technology presents high efficiency, with the values like 80% or higher, when the considered energetic production is the sum of the electrical one with the heat used to produce electricity by conventional ways, like thermal turbines generators. Figure 1.3 shows that the SOFC is the one with the higher power-producing, as required for electric generation stations to supply the electrical grid when the production of electricity by renewable sources is insufficient [6].

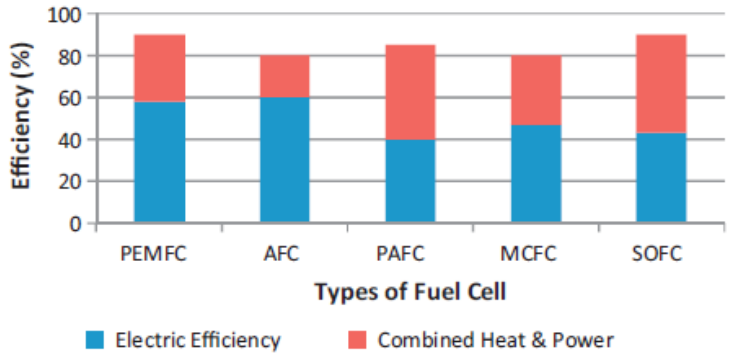


*Figure 1.2. Fuel cell efficiency for: Proton Exchange Membrane Fuel Cell (PEMFC); Alkaline Fuel Cell (AFC); Phosphoric Acid Fuel Cell (PAFC), Molten Carbonate Fuel Cell (MCFC) and Solid Oxide Fuel Cell (SOFC) [6].*

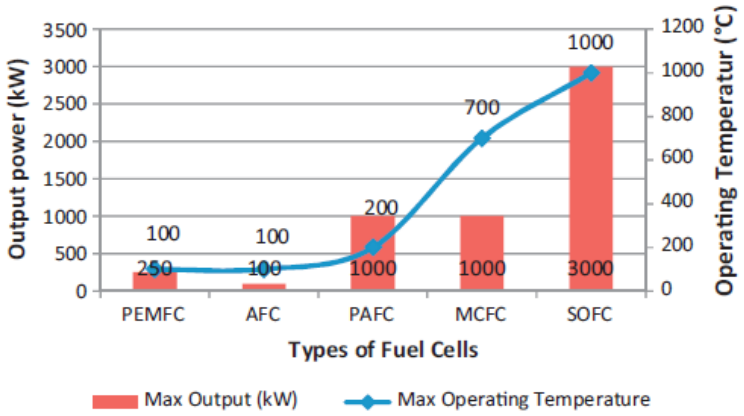


*Figure 1.3 Output power for different fuel cells: Proton Exchange Membrane Fuel Cell (PEMFC); Alkaline Fuel Cell (AFC); Phosphoric Acid Fuel Cell (PAFC), Molten Carbonate Fuel Cell (MCFC) and Solid Oxide Fuel Cell (SOFC) [6].*

## 1.2 Alkaline Water Electrolysis

Alkaline Water Electrolysis is a low-temperature process, in which the electrolyte is an alkaline solution (pH>7). Due to the low operation temperature, around 70 to 100 °C [2], the degradation of catalyst materials is mitigated by slow kinetics. However, low operation temperature also results in an increase of the overvoltage for hydrogen evolution reaction eq. 1.1) and oxygen evolution reaction eq. 1.2), increasing the potential difference required for each reaction to proceed, and decreasing the electrolyser cell efficiency to approximately 60% [7].

$$4H_2O + 4e^- \rightarrow 4OH^- + H_2 \qquad \text{eq. 1.1)}$$

$$4OH^- \rightarrow 2H_2O + 4e^- + O_2 \qquad \text{eq. 1.2)}$$

Figure 1.4 is a scheme for an alkaline electrolyser, the hydrogen production occurs at the cathode in which hydrogen in reduced from $H_2O$ to $H_2$ and $OH^-$ is formed under cathodic polarization as described by eq 1.1). At the same time, at the anode, $O_2$ is formed by the oxidation of $OH^-$, as described by eq 1.2), drawing the migration of $OH^-$ from the cathode to the anode. A diaphragm may be included between the electrodes, in the liquid electrolyte, that is permeable to the $OH^-$, but impermeable to the gases, acting as a separator between $H_2$ with $O_2$ for their individual recovery [3].

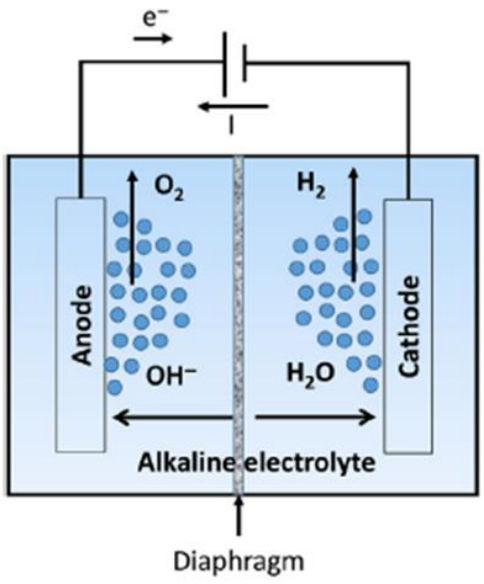


*Figure 1.4. Scheme of an alkaline electrolyser [2].*

The development of the alkaline water electrolysis is focused on the efficiency boost and on increasing the hydrogen production rate [8]. The efficiency improvement can be achieved by decreasing the cell overvoltage, by the incorporation of the catalyst materials in each electrode. In order to ensure the applicability at larger scales, a promising direction involves the development of electrodes free of platinum group metals.

As the efficiency, the hydrogen producing rate can be increased by diminishing the bubble interferences. During the operation, gas bubbles are formed at the electrode surface, detaching when they reach a certain size. If the electrode surface is covered with bubbles, the contact between the electrode and electrolyte is reduced, increasing the cell overvoltage. The solutions for this problem include mechanical circulation of the electrolyte, that will force the bubbles to detach or by system adjustments to increase the wettability on the electrode surface by electrolyte. In this way, the electrode will attract the electrolyte solution while the bubbles are repealed; this could be achieved through the use of additives that reduces the surface tension of the electrolyte solution and by modification of electrode surface to add a more hydrophilic character to those [7].

### 1.2.1 Components of alkaline water electrolyze cell.

The electrolyte commonly used for alkaline water electrolysis is a solution of KOH [7] or NaOH, their concentrations vary with the working temperature. However, it is generally 25 wt% to 30 wt% for the temperature range of 70 °C to 100 °C [2].

The diaphragm is a microporous material, usually made from asbestos, although it is toxic, and from fibres glass or porous carbon [9]. The average pore size is lower than 1 µm, permitting the migration of $OH^-$ form the cathode to anode, and separation the gases. If the separation of the gas species is inefficient, they can react to produce water, and the risk of explosion is a real concern since this mixture is highly flammable [2].

The electrodes materials must have high catalytic activity, high active surface, high electronic conductivity, high chemical and electrochemical stability [3], for the electrochemical reactions to be feasible, in which the Pt [10] and $IrO_2$ [8], [10] or $RuO_2$ [8] are the materials with the best properties to be applied on cathode and anode, respectively. However, those are highly expensive and rare, impeding their application at a larger scale. The transition metal oxides as Ni, Co, Fe and Mn are stable in alkaline conditions and possess good catalytic activity, being cheaper and more abundant than the noble metals [10].

A typical cathode material for alkaline water electrolyser is Ni, due to its high catalytic activity and low price. However, to maximize Ni electrode activity, it must be nanostructured. Relevant example includes Nickel Raney alloy produced by leaching the Al or Zn content of the NiAl or NiZn precursor alloys, respectively, in a caustic solution creating a highly porous material [11]. Mo addition also improves the catalytic activity in the nanostructures, e.g., the Ni-Mo alloy catalyst for the HER, with a high catalytic activity [12], having high corrosion resistance and electrochemical stability [10].

A good example of the anode material with high activity without platinum group metals is the cobalt spinel $Co_3O_4$ [13]. These are usually supported on Nickel Raney matrix [8], [14]. Since the $Co_3O_4$ phase presents high resistivity, it is doped with Li or La to improve the conductivity, or mixed oxide as $NiCo_2O_4$ [2]. Also the perovskite oxides such as $LaCoO_3$, $LaNiO_3$, $LaMnO_3$ are promising materials for the oxygen evolution reaction, in particular, those substituted with Sr. In particular, the Sr- containing $La_{0.6}Sr_{0.4}CoO_3$ demonstrates one of the highest catalytic activities [15].

## 1.3 Reversible Solid Oxide Fuel Cell

A Reversible Solid Oxide Fuel Cells (RSOFC) operate reversibly from the Solid Oxide Fuel Cell (SOFC) mode to Solid Oxide Electrolyser Cell (SOEC) mode. It is a feasible alternative for energy storage using hydrogen as an energy carrier, to fill time gaps between the availability of renewable electricity and consumption. In SOFC mode, it can generate electricity and heat by the electrochemical combination of air with a fuel such as $H_2$ or syngas. These fuels can be generated in SOEC mode, by electrolysis of $H_2O$, $CO_2$ or $H_2O$ + $CO_2$, using excess of electricity at periods of lower consumption [16]. This is described by eq. 1.3) and eq. 1.4) for electrolysis of steam and, or eq. 1.4) and eq. 1.5) for electrolysis of $CO_2$. In SOFC mode the reactions are reverted from right to left.

$$H_2O + 2e^- \leftrightarrow O^{2-} + H_2 \quad \text{eq. 1.3)}$$

$$O^{2-} \leftrightarrow \frac{1}{2}O_2 + 2e^- \quad \text{eq. 1.4)}$$

$$CO_2 + 2e^- \leftrightarrow O^{2-} + CO \quad \text{eq. 1.5)}$$

Figure 1.5 shows a schematic representation of RSOFC operation in the SOFC and SOEC modes. For the SOFC, and considering $H_2$ as fuel, the principle of operation is straightforward: the fuel is oxidized to steam ($H_2O$), at the fuel electrode, releasing electrons to an external circuit. At the same time, by the supply of electrons, $O_2$ is reduced to $O^{2-}$ ions, at the porous air electrode; this also draws $O^{2-}$ ions through the electrolyte from the air electrode/electrolyte interface to the interface electrolyte/fuel electrode interface. For the SOEC mode, $H_2O$ is reduced to $H_2$ at the fuel electrode, under cathodic polarization, drawing $O^{2-}$ from the fuel electrode/electrolyte interface to the electrolyte/air electrode, and oxidising these ionic species at the air electrode under anodic polarization.

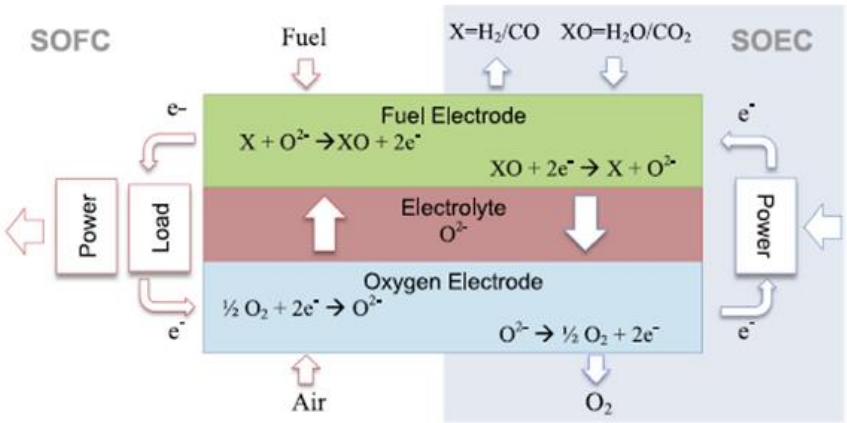


*Figure 1.4. Operating RSOFC principles: SOFC and SOEC modes [16].*

The development of RSOFC technology is practically focused on the research of new materials to prevent performance losses or degradation of electrodes or electrode/electrolyte interfaces. Degradation may be caused by different phenomena such as expansive transformations or chemical expansion induced by redox changes, microstructural changes such as coarsening of metallic components at relatively high operating temperatures, contamination of electrode materials with impurities from fuels (e.g. sulphur), deposition of carbon at the fuel electrode when

hydrocarbons or syngas are used as fuels, delamination or structural changes induced by impurities or inter-diffusion between different cell layers or oxygen pressure build-up in electrolysis mode, mainly when current density is high (>1Acm$^{-2}$ ) [16].

### 1.3.1 Components of Reversible Solid Oxide Fuel Cells

The classical electrolyte materials of solid oxide fuel cells is yttria stabilized zirconia (YSZ), due to its combination of ionic conductivity, thermochemical and mechanical stability and wide electrolytic domain. Other potential solid electrolytes such as ceria-based materials (CGO, CSO,…) are ill-suited mainly for their reducibility, which raises concerns about applicability even in the fuel cell mode, except possibly as a buffer layer to avoid reactivity between YSZ and some oxygen electrode materials [17], [18].

Oxygen electrodes for RSOFC's must present high electrical conductivity, high catalytic activity for oxygen reduction, and compatibility with other cell components, namely, the solid electrolyte. Thus the classical $La_{1-x}Sr_xMnO_{3-\delta}$, (LSM) electrodes are mostly used based on the relatively high electronic conductivity and thermal expansion coefficient that match the YSZ electrolyte [16], without requiring buffer layers. Still, LSM is prone to severe degradation, mainly by delamination under high anodic overpotential; this causes sudden failure ascribed to cation de-mixing induced by oxygen excess, i.e., $La_{1-x}Sr_xMnO_{3-\delta}$, causing sudden failure after the operation in electrolysis mode for about 100 h at 750 °C with 1.5 Acm$^{-2}$ [19]. Degradation may be minimized or even reverted on cycling between electrolysis and fuel cell modes, before reaching the incubation time for formation of new phases or voids [16]. Other authors reported stable performance for oxygen electrodes with high oxygen excess ability such as $Ln_2NiO_4$, Ln=La, Pr,… [20]; this required a buffer layer to prevent reactivity with YSZ.

Usually, the material used as fuel electrode for RSOFCs is still a Ni-YSZ cermet, where Ni exhibits a high catalytic activity toward the oxidation of hydrogen, and it is also active for internal reforming of hydrocarbon fuels. It is a good electronic conductor, and its cost is affordable. The YSZ provides an ionic pathway for $O^{2-}$, acts like a skeleton to prevents sintering of nickel, and allows closer thermal expansion matching with the YSZ electrolyte. Still, tests in electrolysis mode show that both electrodes contribute to the degradation of performance on increasing current density up to 1.5 Acm$^{-2}$ [16].

The durability of the fuel electrode is mainly determined by the processes occurring during thermal cycles or redox cycles, causing coarsening of the metallic phase, microstructural degradation or even cracking by the expansive onset of NiO. In addition, operation with hydrocarbons raises risks of sulphur poisoning or loss of catalytic activity of the anode due to coking. Ni-YSZ cermet has a low tolerance to sulphur and at high temperatures exhibits high catalytic activity for C-C bond formation, when hydrocarbons are used as fuels; this promotes carbon deposition, isolating the Three-Phase Boundaries (TPB) from the fuel. Usually this is minimized in fuel cell mode by pre-reforming or by addition of large fractions of steam and/or $CO_2$ to the fuel stream. This approach is ill-suited for the electrolysis mode.

Thus, Ni-YSZ-based cermets require tailoring of the composition to enhance performance and to improve sulphuring/ coking resistance. Modifications of the traditional Ni-YSZ cermets are also focused on increasing TPB area by enlarging reaction sites, to promote stability and enhanced catalytic activity by materials substitution, doping, introduction of active layers, and microstructure

refinements. The addition of Fe to the Ni fuel electrode seems effective for improving the SOEC performance, where the potential losses become much larger than in SOFC mode. Another strategy to enhance the performance is impregnating of an ionic conductor (e.g. GDC) with nanoparticles, which increases the active region and decreases the electrode polarization resistance [16]. Cu has been used to replace Ni, achieving higher coke resistance when compared to Ni-YSZ. However, Cu-YSZ cermets present lower conductivities after sintering and fast microstructural degradation [16].

### 1.3.2 Mechanisms of fuel electrode degradation

#### *1.3.2.1 Redox Cycling*

The redox cycling degrades the properties of the SOFC due to large volume difference between metallic Ni an oxide Ni, yielding significant strain and cracks or seal leakage, delamination and eventually shut down [21].

Usually, the reduction of NiO to Ni happens in situ, when the SOFC is turned on for the first time, interacting with the reducing fuel. The NiO component of the as fired NiO-YSZ composite is reduced to much denser Ni, whereas the YSZ skeleton prevents major volume changes. Thus, reduction contributes to increasing the final porosity of the Ni-YSZ cermet [22], promoting access to fuels on the Triple-Phases Boundaries.

Assuming that the fuel supply is continuous, the fuel electrode is held in reducing conditions, preventing oxidation of its metallic component (Ni). However, if the fuel supply is interrupted (either intentionally or as the result of a fault), oxygen may crossover through leaks or cracks in the electrolyte and re-oxidise Ni to NiO. This oxidation is accomplished by an increase of volume causing expansion of the fuel electrode. When the fuel supply is again turn on, the anode will be exposed again to a reductive atmosphere and the NiO will reduce to Ni metallic without complete recovery [22].

Thus, the dimensional changes can be built up over many redox cycles, generating internal strain on the fuel electrode and also on other thinner cell components, eventually causing cracks, losses of performance, or even complete loss of integrity. Table 1.1 reveals the dimensional accumulation through 3 redox cycles, measured by relative length change ($\Delta l / l_0$) of NiO/YSZ bars in redox cycling at 1000 °C. The influence of yttria content in YSZ is also shown [22]. With the strain accumulation cracks may occur, extending readily through the thin electrolyte layers, as shown in figure 1.5 [22].

*Table 1.1. Relative length change ($\Delta l / l_0$) of Ni-YSZ bar specimens in redox cycling experiments at 1000 °C showing the influence of yttria content in the YSZ [22].*

| Redox step | 8YSZ | 3YSZ |
|---|---|---|
| 1st reduction | 0.00 | 0.00 |
| 1st oxidation | 1.19 | 0.35 |
| 2nd reduction | –0.22 | –0.08 |
| 2nd oxidation | 2.44 | 0.70 |
| 3rd reduction | –0.24 | –0.01 |
| 3rd oxidation | 2.13 | 0.67 |
| Total | 5.30 | 1.63 |

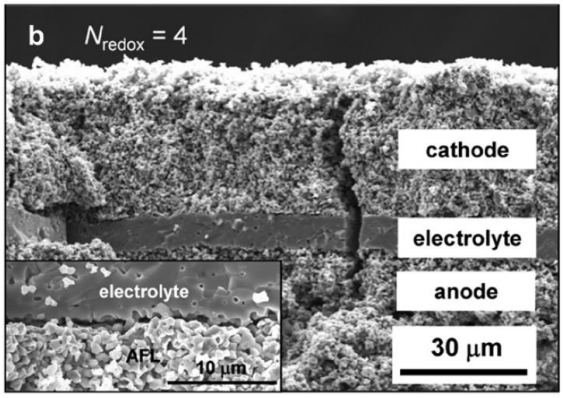


*Figure 1.5. SEM image of the fuel electrode-supported tubular cell after 4 redox cycles [23].*

The cell voltage also changes on redox cycling, as shown in figure 1.6. The arrows indicate the point at which each redox cycle occurs and the oxidation time, while the line indicates the initial cell voltage and the measured cell voltage after each redox cycle. After each oxidation, the cell underwent 4 hours of reduction atmosphere to recover from the oxidation, before the starting of cell voltage measurement [21]. Degradation is limited in the first redox cycle, but faster degradation is observed after few redox cycles. Thus, reversibility is not enough for complete recovery.

One must also take into account that the extent of degradation of anode-supported SOFCs depends mainly on the degree of oxidation of the thick supporting layer [24], rather than the effective anode, consisting of a much thinner electrocatalytic layer. Thus, enhanced redox tolerance may be attained by acting preferentially on the supporting or electrocatalytic layers, including changes in the composition of ceramic or metallic phases of cermets and their interactions or microstructural design.

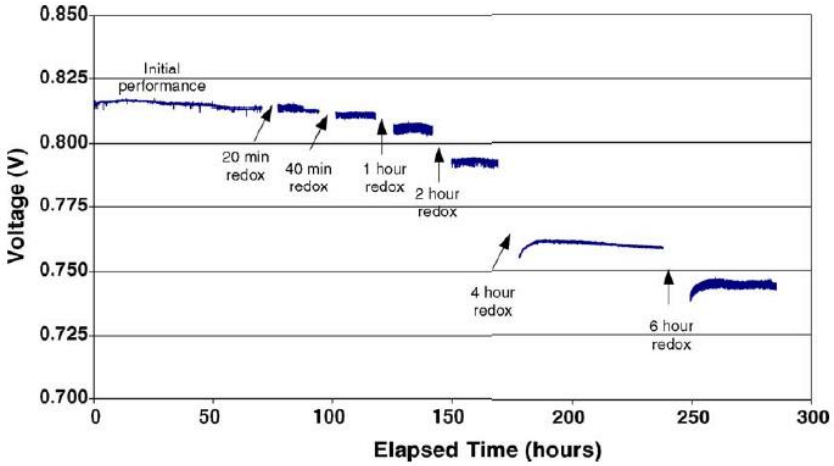


*Figure 1.6. Cell voltage Vs. Redox cycling. The tests were performed at 750 °C and 0.5A/cm² in humidified hydrogen [21].*

### *1.3.2.2 Coking*

To operate a SOFC on hydrocarbons, its fuel electrode should combine activity for the required reactions of fuel reforming and electrochemical oxidation, while preventing coke formation [25]. Nickel-based cermets have good catalytic activity and stability for reforming low molecular weight hydrocarbons but tend to suffer from coke formation and sintering, mainly with higher molecular weight fuels. Both are detrimental to the long-term stability of the fuel cells. Nevertheless, highly dispersed Ni nanoparticles exhibit much-improved reforming activity, higher stability and lower coke formation. On Ni-based anodes, coking begins with carbon nucleation, and the low metallic dispersion of supported Ni catalysts has been recognized as one of the reasons for poor tolerance to carbon deposition [25]. So, the prevention of Ni nanoparticle to agglomerate is a very critical step to prevent coking during internal reforming of hydrocarbon fuels.

Modifying the catalyst support and introducing additives can improve the activity and stability of Ni catalysts. The interaction between the active metal and the support affects the catalyst performance by changing the properties of the active phase such as its reducibility and dispersion [25]. For example, it has been reported that the presence of molybdenum enhances the long-term stability of the Ni-based catalyst by strengthening the interaction between Ni and the support and improving the overall metal dispersion [25]. The presence of Mo maintains the small size of the Ni particles as shown by TEM/EDS in figure 1.7 for a Ni-Mo(3%)/ceria-zirconia cermet, and hinders coke formation [25].

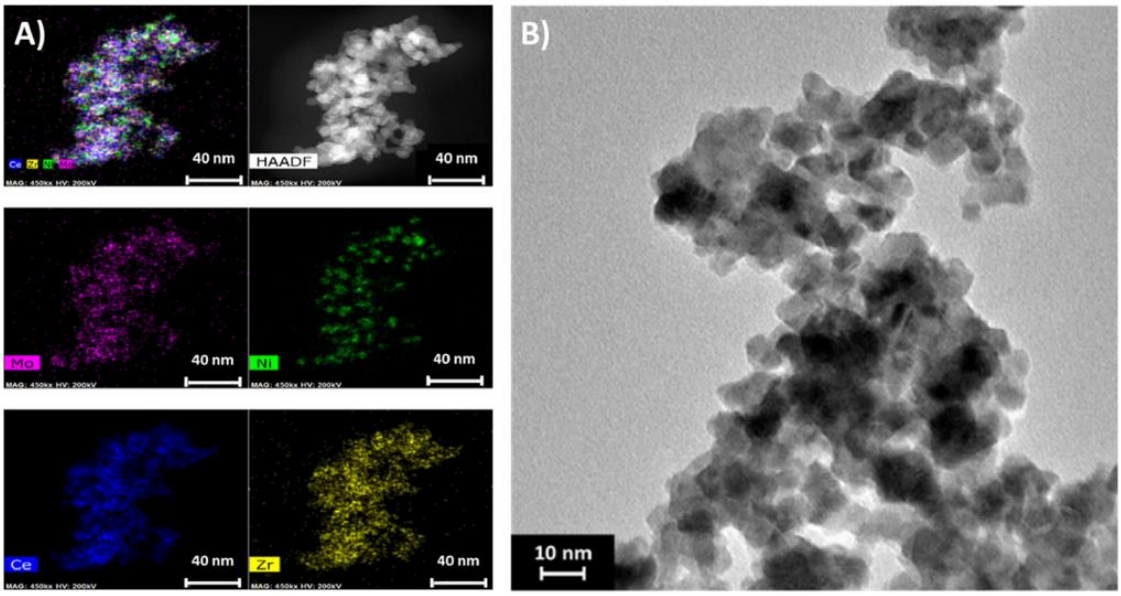


*Figure 1.7. Scanning transition electron microscopy with EDS on Ni-Mo(3%)/CZ sample (A), and its transmission electron microstructure (B). [25]*

By comparing XRD patterns of samples without [Ni/CZ] and with 3 wt% Mo addition [Ni-Mo(3%)/CZ] (figure 1.8), one also observes structural effects of Mo addition before and after catalytic testing in partial oxidation of isooctane. The XRD of Ni-Mo(3%)/CZ catalysts are similar before and after catalytic testing, whereas the catalyst without Mo [Ni/CZ] shows sharper peaks, indicating increase of crystallite size, an also onset of a new diffraction peak, at approximately 26 °, corresponding to graphitic carbon formation [25].

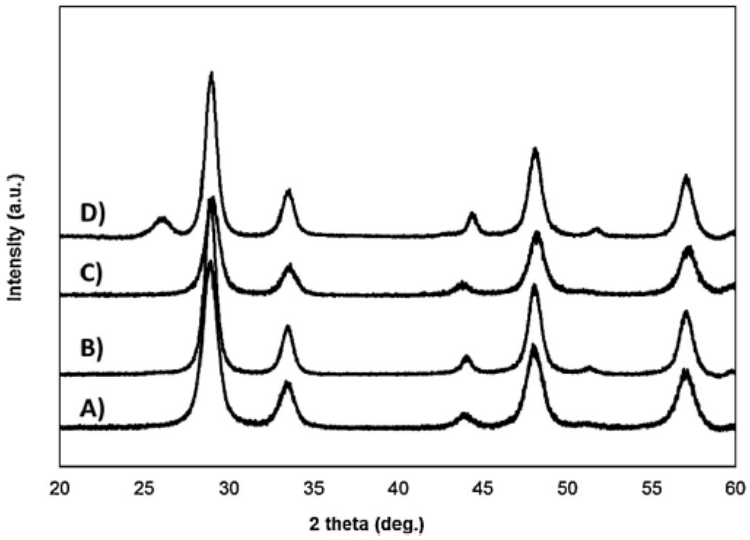


*Figure 1.8. XRD patterns of Ni-Mo(3%)/CZ (A and B) and Ni/CZ (C and D) before operation (A and C) and after operation in contact with isooctane (B and D). The operation time for Ni-Mo (3%)/CZ sample was 24 hours, while that of Ni/CZ was less than 4 hours, duo to severe fuel cell degradation. [25]*

The effect of Mo on the performance of catalytic reforming, figure 1.9, was also studied at constant current density of 0,5 $Acm^{-2}$ and at 750 °C. The single cell without the catalyst layer showed an unstable voltage and the overall cell performance exhibited a rapid degradation. The fast degradation could be due to carbon deposition in the anode. The corresponding single cell with catalytic layer displayed significantly improved stability with a low degradation rate. The improved performance demonstrated positive role of catalytic layer on reforming of complex hydrocarbon fuels and suppression of carbon deposition [25].

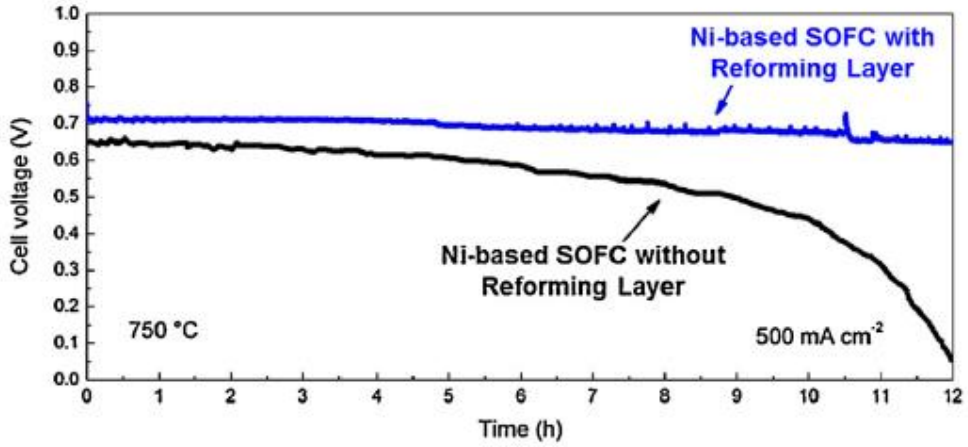


*Figure 1.9. Performance stability of the Ni-YSX anode-based SOFC with the Ni-Mo(3%)/CZ catalyst layer at the constant current density of 0,5 $Acm^{-2}$ [25].*

Ni-Ti-O is also a promising system to design catalysts or fuel electrodes with carbon tolerance, as found on impregnating the Ni-YSZ fuel electrode with $NiTiO_3$ (NTO) [26]; this effect was related to the decomposition of NTO to Ni and $TiO_2$, under reducing conditions, promoting steam reforming of hydrocarbons and hindering carbon deposition. Besides, it was suggested that formation of oxygen vacancies in reduced $TiO_2$ also contribute to the reforming reaction and to carbon inhibition [26].

$TiO_2$ was also reported as a stabilizing support for a variety of heterogeneous catalysts or electrocatalysts, designed to operate in different electrochemical environments [27]. For electrochemical or catalytic applications at relatively low temperatures, one may rely on pure anatase phase, with sharp pore distribution and large surface area, and ability to increase the degree of distribution and homogeneity of immobilized catalysts, resulting in improved stability and catalytic activity. For example, $TiO_2$ – supported catalysts may combine electrocatalytic performance and outstanding resistance towards corrosion in different electrolytic media. Alternatively, titania may be reduced to different Magnéli phases $Ti_nO_{2n-1}$. These phases remain metastable and possess relatively high electrical conductivity at room temperatures, which makes them suitable as catalyst supports for the oxygen reduction reaction, and for hydrogen/oxygen evolution.

High-temperature applications cannot rely on anatase, which transforms to rutile. Still, $Ni/TiO_2$ interfaces may hinder undue coarsening of Ni particles in Ni-based cermets, maintaining their percolation and current collection to relatively low fractions [28]. Similarly, Magnéli phases

cannot rely on metastability at representative temperatures of SOFC, but may still be expected in electrolysis mode, namely in very dry $H_2$, and or under cathodic polarization.

## 1.4 Redox thermodynamics of electrodes and fuels

### 1.4.1 Guidelines from Ellingham diagrams

Thermodynamics may provide useful predictions for the redox conditions during RSOFC operation on changing from fuel cell mode to electrolysis mode. High conversion of fuels in the fuel cell mode corresponds to the high ratio of oxidized to reduced species, i.e., for $H_2O{:}H_2 \gg 1$ or $CO_2{:}CO \gg 1$, whereas electrolysis is expected to yield fuels with low moisture and/or low $CO_2$ contents, i.e., $H_2O{:}H_2 \ll 1$ or $CO_2{:}CO \ll 1$. Thus, reversibility imposes significant changes in redox conditions, which may be described by the classical Ellingham diagram [29] for equilibrium redox pairs such as Ni/NiO; this is described by eq. 1.6), as shown in figure 1.10, where *ΔG* is the free energy of reaction between the redox pair (e.g., $2Ni + O_2 \leftrightarrow 2NiO$):

$$RTln(pO_2) = \Delta G \qquad \text{eq. 1.6)}$$

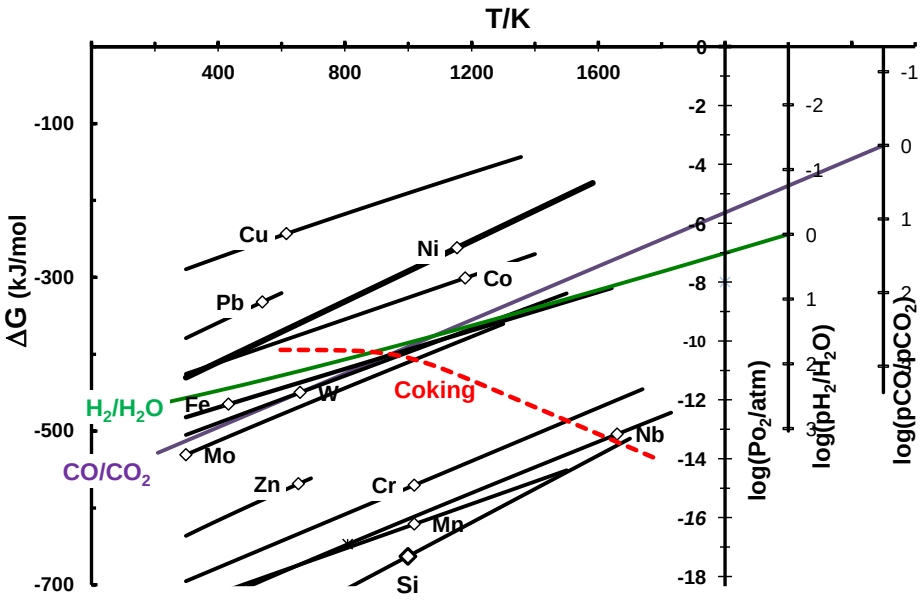


*Figure 1.10. Section of Ellingham diagram redrawn [29].*

In addition, the Ellingham diagram shows the redox conditions for oxidation of $H_2$, i.e., for reaction $2H_2 + O_2 \Leftrightarrow 2H_2O$. In this case, the redox conditions in the fuel also depend on the ratio of oxidised to reduced species, as shown in eq. 1.7):

$$RTln(pO_2) = \Delta G + 2RTln\left(\frac{pH_2O}{pH_2}\right) \qquad \text{eq. 1.7)}$$

### 1.4.2 Thermodynamics of $H_2/H_2O$ mixtures in fuel cell and electrolysis mode

Figure 1.11 shows a transformation of the Ellingham diagram to facilitate the direct reading of oxygen partial pressure of relevant redox pairs and their temperature dependence; this is readily obtained by transforming eq. 1.6) into eq. 1.8):

$$log(pO_2) = \frac{\Delta G}{2.30RT} \qquad \text{eq. 1.8)}$$

Similarly, for the redox conditions in the fuel $H_2$ / $H_2O$, the eq. 1.9), this is obtained by the transformation of the eq. 1.7):

$$log(pO_2) = \frac{\Delta G}{2.30RT} + 2log\left(\frac{pH_2O}{pH_2}\right) \qquad \text{eq. 1.9)}$$

Thus, one may assess prospects to retain the redox stability of selected metal/oxide pairs such as Ni/NiO and $Mo/MoO_2$, under the reduced conditions imposed by the fuel.

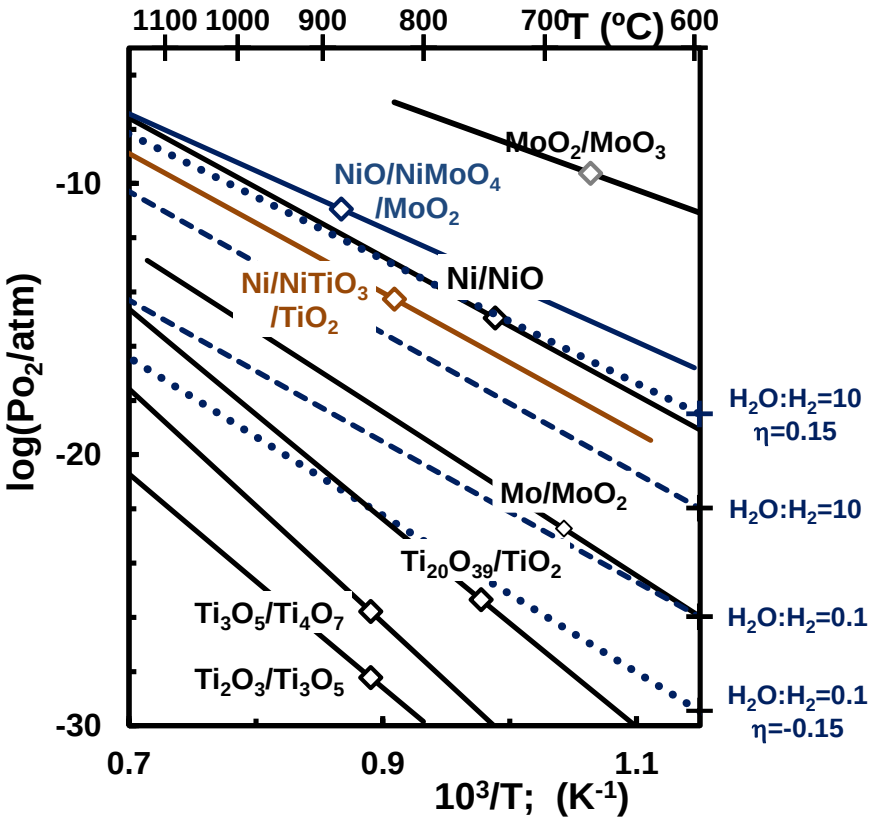


Figure 1.11. *An alternative representation of Ellingham diagram for Ni/NiO, $Mo/MoO_2$ and other redox pairs or 3-phase equilibria in the Ni-Mo-O and Ni-Ti-O systems. The dashed lines show $H_2O/H_2$ equilibrium for the indicated values of $H_2O/H_2$ ratio and dotted lines show corresponding predictions with representative values of anodic or cathodic overpotential.*

Figure 1.11 also shows the differences in redox conditions on reverting from fuel cell mode, with prevailing oxidised species, to electrolysis mode, with prevailing reduced species. These

conditions are simulated in figure 1.11 for $(H2O:H_2)_f = 10$ in fuel cell mode and $(H_2O:H_2)_e = 0.1$ in the electrolysis mode, yielding differences between the oxygen partial pressure for fuel cells and electrolyser. In addition, the fuel electrode reverts from anodic polarization in fuel cell mode ($\eta_a > 0$) to cathodic polarization in electrolysis mode ($\eta_c < 0$), where the overpotential is given by the Nernst equation, eq. 1.10):

$$\eta = \frac{RT}{4F} ln\left(\frac{pO_{2,\eta}}{pO_{2,o}}\right) \quad \text{eq. 1.10)}$$

Thus, fuel cell operation occurs in even less reducing conditions, whereas cathodic polarization in electrolysis mode imposes more severe reducing conditions, as described by eq. 1.11):

$$log\left(pO_{2,\eta}\right) = \frac{\Delta G}{2.30RT} + 2log\left(\frac{pH_2O}{pH_2}\right) + \frac{4F\eta}{2.30RT} \quad \text{eq. 1.11)}$$

In this case, the modified Ellingham diagram shows typical conditions when the $H_2$-based atmosphere may still be insufficient to sustain redox stability for metallic Ni, namely, relatively high fuel conversion and significant anodic overpotential, in fuel cell mode.

Redox conditions for $Mo/MoO_2$ are also shown in figure 1.11, to seek the incorporation of Ni-Mo or Ni-Mo-O electrocatalysts in fuel electrodes, based on evidence of catalytic activity [25], [30], and also tests of Ni-Mo-Ceria-Zirconia SOFC anodes [31], [32]. The redox stability of metallic Mo is limited, except in electrolysis mode. Still, Mo is soluble in Ni-based alloys (figure 1.12) for up to about 18 at% at typical SOFC operating temperatures (<900 °C); this suppresses the activity of Mo and may prevent its oxidation even in fuel cell mode, mainly for very small contents of Mo (<5%), when its activity coefficient is lower than unit [33]. The activity coefficient rises sharply for contents of Mo in the order of 20%, i.e., at the onset of the intermetallic phase $Ni_4Mo$ (figure 1.12).

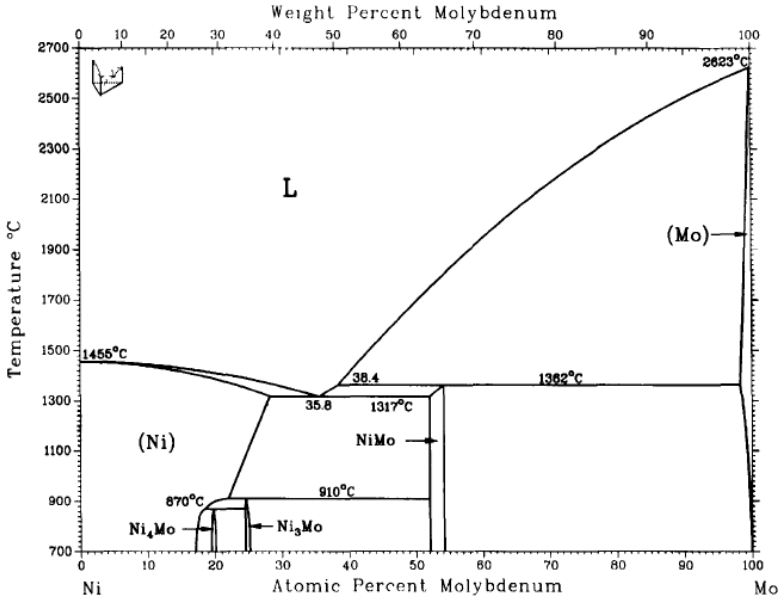


*Figure 1.12. Phase diagram of Ni-Mo system [34].*

$NiMoO_4$ has also been proposed as a potential catalyst for fuel conversion reactions such as oxidative de-hydrogenation [35]. Its redox stability is limited by decomposition, as shown in eq. 1.12):

$$2NiMoO_4 \Leftrightarrow 2NiO + 2MoO_2 + O_2 \qquad \text{eq. 1.12)}$$

and was assessed by solid state electrochemical cells [33], yielding as described by eq. 1.13):

$$log(pO_2) = 33.31 - \frac{48399}{T} \qquad \text{eq. 1.13)}$$

This redox stability limit is also shown in figure 1.11, to emphasize that this is out of the expected redox range of fuel cells and electrolysers, except possibly for fuel cell mode with excessive cathodic polarization. Thus catalytic activity for de-hydrogenation of hydrocarbons may depend on metastability of $NiMoO_4$, at relatively short time scales, or subsequent redox behaviour of resulting oxides ($2NiO \Leftrightarrow 2Ni + O_2$ or $MoO_2 \Leftrightarrow Mo + O_2$), rather than the defect chemistry of $NiMoO_4$, as claimed in reference [35].

$NiTiO_3$ is also considered for the proposed fuel electrodes, based on expected effects on reforming reactions [36] and inhibition of carbon deposition [37], possibly involving spontaneous decomposing in contact with fuels, yielding active Ni / $TiO_2$ interfaces, as described in eq. 1.14):

$$2NiTiO_3 \Leftrightarrow 2Ni + 2TiO_2 + O_2 \qquad \text{eq. 1.14)}$$

Ni / $TiO_2$ interfaces are also expected to hinder undue coarsening of Ni particles and loss of their percolation [28]. Thus, figure 1.11 also shows the 3-phase equilibrium for $NiTiO_3$ – Ni – $TiO_2$ [38] to confirm close matching between the ternary point and redox conditions in SOFC mode.

One may also consider onset of $Ti_nO_{2n-1}$ Magnéli phases in reducing atmospheres [39]. Thus, figure 1.11 shows predictions for representative pairs of Magnéli phases, based on thermodynamic data [40]. However, thermodynamic predictions indicate that this requires very dry $H_2$, combined with significant cathodic polarization in electrolysis mode, even for the end member of the identified Magnéli phases $Ti_{20}O_{39}$. Otherwise, onset of other commonly reported phases (e.g., $Ti_4O_7$) should require a combination of very dry $H_2$ and higher temperatures [38], i.e., well above operating conditions of SOEC.

### 1.4.3 Thermodynamics of CO:$CO_2$ mixtures in fuel cell and electrolysis mode

The thermodynamics of CO:$CO_2$ mixtures, eq. 1.15), is similar to that of $H_2$:$H_2O$, i.e.:

$$log(pO_{2,\eta}) = \frac{\Delta G}{2.30RT} + 2log\left(\frac{pCO_2}{pCO}\right) + \frac{4F\eta}{2.30RT} \qquad \text{eq. 1.15)}$$

The main difference is related to risks of carbon deposition described on combining the mass action constants by eq. 1.16) and eq. 1.17):

$$2CO + O_2 \Leftrightarrow 2CO_2 \qquad \text{eq. 1.16)}$$

$$2CO \Leftrightarrow C + CO_2 \qquad \text{eq. 1.17)}$$

This is represented by the dashed-dotted line in figure 1.13 and emphasizes risks of carbon deposition in the electrolysis mode, mainly at temperatures below 900 °C, also emphasizing that fuel electrodes with carbon tolerance are needed mainly if one considers electrolysis of $CO_2$ or co-electrolysis of $CO_2$ and steam. Interestingly, one finds close matching between the redox Mo/$MoO_2$ pairs and thermodynamic conditions for onset of carbon at about 750 °C, possibly contributing to explain the role of Mo in carbon-tolerant catalysts and electrocatalysts. The catalytic or electrocatalytic activity of $NiMoO_4$ - based catalysts may even be more complex as revealed by Post-Morten XRD after dry reforming reactions, which showed onset of reduced Ni, possibly alloyed with Mo, and also partially reduced $MoO_2$ and even a carbide phase ($Mo_2C$) [41].

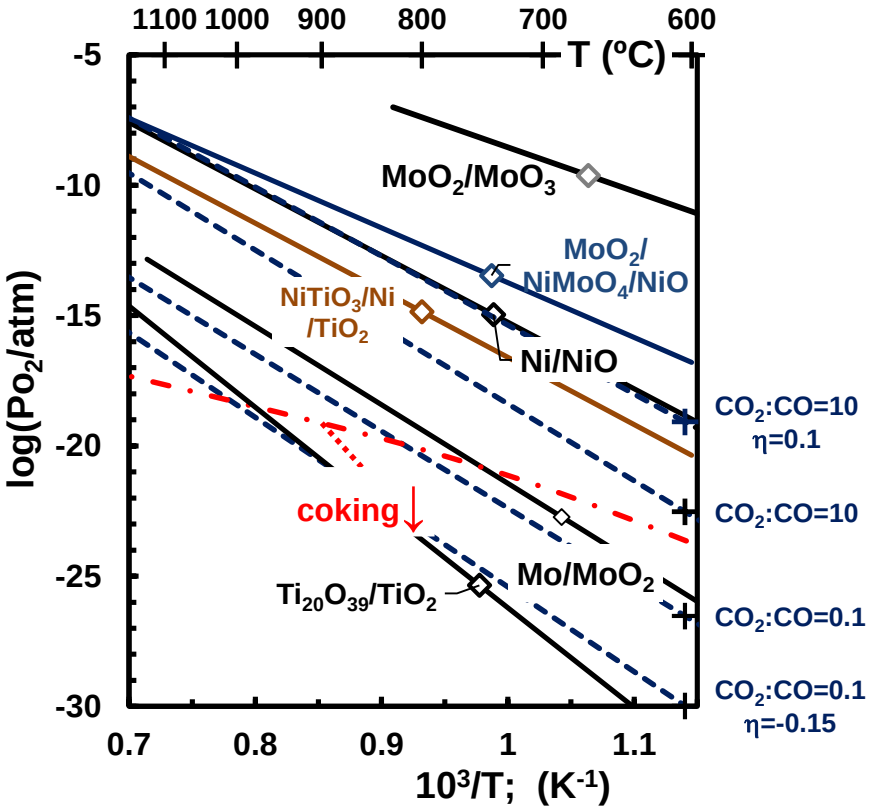


*Figure 1.13. An alternative representation of Ellingham diagram for electrodes based on the Ni-Mo-O and Ni-Ti-O systems and redox conditions for $CO/CO_2$ mixtures. The dashed lines show $CO/CO_2$ equilibrium for the indicated values of $CO_2$:CO ratio and dotted lines show corresponding predictions with representative values of anodic or cathodic overpotential. Conditions for onset of carbon deposition are denoted by the dashed-dotted line.*

# 2 Experimental

## 2.1 Synthesis of the precursor powders

The processing method used for the synthesis of the precursors powders was the Pechini method. The reactants were dissolved in an organic matrix (citric acid) creating a metal-citrate complex, which was then solidified by the polymerization reactions with a diol (ethylene glycol). This was followed by the burning of organics to form the ashes with a mixture of the intended oxides with carbonates, with subsequent calcination step to release the remaining carbon.

During the dissolution of the reactants in the organic matrix, the cations were well homogenised in the solution and trapped by the polymerization reactions impeding their segregation. The composition of the oxide is expected to be homogeneous, just as the cations distribution in the organic matrix. Also, the powder produced is expected to be nanostructured due to the cations segregation only occurs during the combustion.

The intended compositions of the target precursor powders were $NiTiO_3$; 90 at% $NiTiO_3$ +10 at% $MoO_3$ and 80 at% $NiTiO_3$ + 20 at% $MoO_3$, designated in this work by NTO powder, 0.9NTO powder and 0.8NTO powders respectively. The reactants used were nickel (II) oxide from (99%, Alfa Aesar); titanium (IV) isopropoxide (≥97.0%, Sigma-Aldrich) and ammonium molybdate tetrahydrate (≥99.0%, Fluka Analytical). For the formation of the organic matrix one used citric acid (≥99.0%, SIGMA-ALDRICH) and ethylene glycol (≥99.5%, Fluka Analytical).

The synthesis of the compositions containing molybdenum by Pechini method was started from the dissolution of nickel oxide in nitric acid, this was used in excess to speed up the dissolution, at approximately 180 °C (temperature of the hotplate) with magnetic stirring. After the dissolution, the remaining nitric acid was decomposed on evaporation, the solution (nickel dissolved in nitric acid) reached a viscous aspect as show in figure 2.1 a). Next, distilled water was added until homogenization, followed by the addition of citric acid and ammonium molybdate tetrahydrate until their complete dissolution. After their dissolution, the stoichiometric amount of titanium (IV) isopropoxide was added, and the suspension was left overnight at 150 °C for the complete dissolution of titanium (IV) isopropoxide. After homogenization, the excess of water was removed by heating the hotplate up to 230 °C. Finally, the ethylene glycol was added to start the polymerization reaction. During the polymerization reaction, the temperature and the rotation speed of the magnetic stirrer had to be adjusted to assure the conciliation between the homogenisation of ethylene glycol on the citric acid, with the cations dissolved, without the foam formation. In the beginning, the temperature had to be constant, with lower rate of magnetic stirring, to impede the foam formation, as possible to observe in figure 2.1 b). The foam was formed by the water evaporation, and when the evaporation was almost completed the temperature was increased gradually, and the speed of magnetic stirrer rotation was decreasing until the solution reached a viscous texture, as show in figure 2.1 c), in which the magnet had difficulty to rotate, and was removed before sticking.

After the solidification, one proceeded with the partial combustion of the organic matrix by the gradual increase of the temperature until 400 °C, figure 2.1 d). The heating was relatively slow to prevent the glass break. After the partial combustion, the remains are ashes as shown in figure 2.1 e). Next, the ashes were ground in a mortar with ethyl alcohol and dried in an oven to obtain the powders, as represented in the figure 2.1 f). For the NTO powder without molybdenum, the

procedure was the same except the step of adding and homogenization of ammonium molybdate tetrahydrate.

In order to obtain the precursor powder without carbon residues, as show in figure 2.1 g), the powders were calcinated in air. For that, the thermal cycle had to be optimized to obtain powders with the intended compositions. The details of the optimization procedure for calcination of the powders are described in the discussion section.

After calcination, the powders were ground again with ethyl alcohol and dried for the following XRD and SEM/EDS analysis.

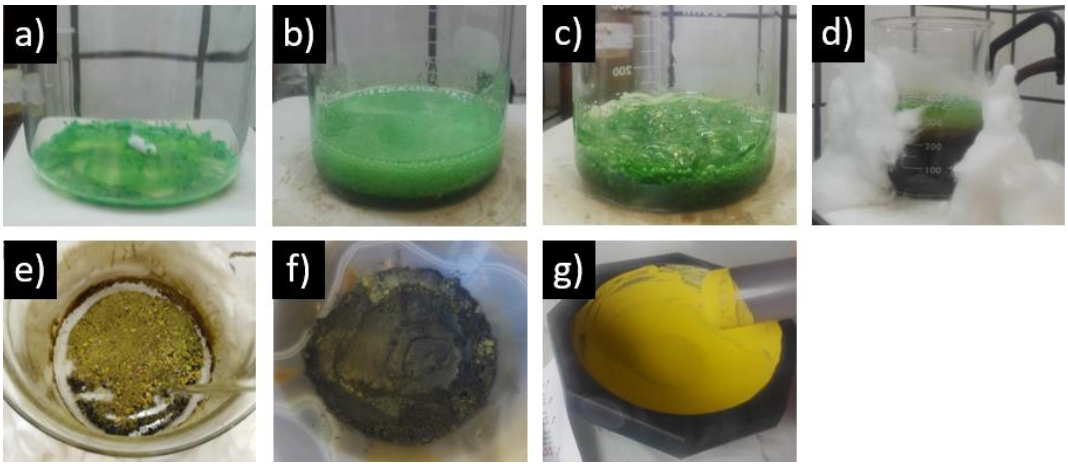


*Figure 2.1. Different steps of the Pechini method. a) dissolution of nickel in nitric acid; b) polymerization reaction beginning and formation of foam, c) polymerization reaction finishing; d) partial combustion; e) material remaining after partial combustion; f) after grounding the ashes of the partial combustion, and g) powder after the calcination.*

## 2.2 Ceramics processing

For comparative studies of the electrical properties at various temperatures, corresponding ceramic samples were prepared by uniaxial pressing followed by sintering.

The uniaxial pressing was performed using a mould of 2 cm diameter, wiped with oil. The amount of powder for each pellet was 2.5 g. For the samples containing Mo, the pressure was ~16 MPa, while for the NTO composition it was ~13 MPa to avoid the formation of cracks. After uniaxial pressing, the samples were subjected to isostatic pressing at 196 MPa, except the one of NTO composition. For the sintering of all composition, the atmosphere used was 10% $H_2$ + 90% $N_2$ at 1300 °C for 5 h and the heating as cooling rate corresponded to 5 °C/min. After sintering, the pellet was cut to form bars for testing the electrical conductivity, phase composition by XRD and microstructural studies by SEM and EDS.

To evaluate the stability of Mo-containing samples in oxidizing conditions, pellets of each composition was produced and sintered in air. To produce those, 0.5 g of each composition was used and pressed only by uniaxial pressing in a mould of 1 cm diameter at ~64 MPa. The pellets were sintered in air at 1200 °C for 5 hours at 5 °C/min as the heating and cooling rate, followed by XRD analyses.

## 2.3 Structural and microstructural characterization of the powder and ceramic samples.

For the XRD analysis, the Philips X'Pert MPD diffractometer (Bragg-Brentano geometry, Cu Ka radiation) was used, with the 2θ range from 10 to 80 ° with 0.0260 of step size and 197.1150 s as scan step size. The ceramics samples were grounded with ethyl alcohol and dried. The obtained XRD data was analysed using FullProf Suite software employing Rietveld refinement.

The SEM analysis was performed using Hitachi SU-70 at accelerating voltage of 15kV. To analyse the powdered sample, a piece of carbon tape was glued to the sample holder for each powder composition, then the powders were deposited at the corresponding carbon tape. Afterwards, the sample holder with the powders was submitted to a high flux of air, to remove the unglued grains, following by carbon deposition. In the case of ceramic samples, the pellets were fractured until obtaining a small piece in which the fractured surface was plane, followed by gluing with carbon cement to the standard sample holder. After the samples were put into the hot-air oven, to dry the cement, following by the carbon deposition.

## 2.4 Electrical conductivity measurements.

The studies of electrical conductivity of the samples, prepared in this work, were performed using 4-probes DC method, taking into account the expected resistance of the samples. For the samples with relatively high electrical conductivity, the use of 4-probes DC method allows to minimize the contribution of contact resistances and local thermal voltages, induced by possible inhomogeneities of the temperature distribution.

The electrical conductivity is obtained as the inverse of the resistivity, normalized taking into account the dimensions of the sample. In other techniques, the resistance calculated is the total one $R_T$, the sum of the sample resistance $R_{Sample}$, with wires resistance, $R_W$, plus contacts resistance $R_C$, as described by eq. 2.1).

$$R_T = {}^{V}/_{I} = R_W + R_C + R_{Sample} \qquad \text{eq. 2.1)}$$

The 4-probes DC technique is divided into two different circuits, as shown in figure 2.2, one that supplies current to the sample and another that measures the voltage difference across a certain length of the sample. The current circuit does not have current losses because the resistances are in series configuration and the current that pass each resistance is the same one. The circuit that measures the voltage difference has some losses, however because of the high resistance of the voltmeter ($10^{12}$ Ω or higher), the current that passes in this one is insignificant, as the voltage drops due to $R_W$ and $R_C$, so the detectable voltage is due to the sample resistance.

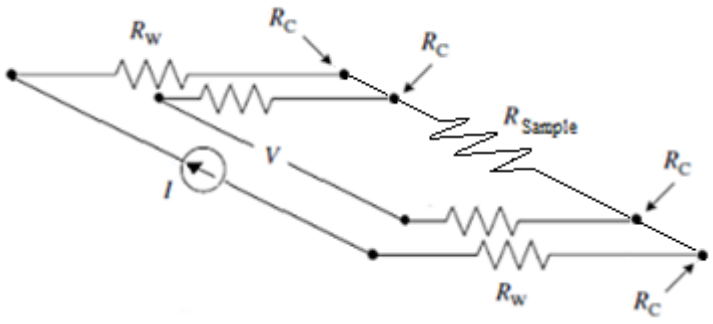


*Figure 2.2. Scheme of the 4 DC probe technique.*

The previously sintered pellets were cut to rectangular bars and polished until all the faces were parallel, with the maximum deviation allowed of 0.03 mm. After polishing, the bar was cleaned in ultrasonic bath with ethyl alcohol. Four Pt wires were then connected to the sample bar for performing 4-probes DC conductivity measurement, as illustrated in figure 2.3 a).

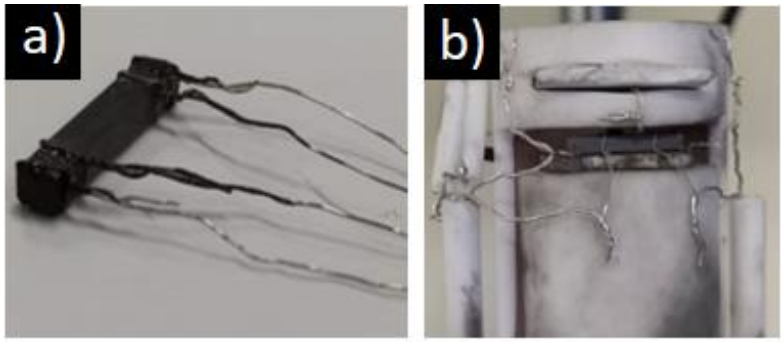


*Figure 2.3. Sample for electrical resistance measurement; and sample connected to the sample holder in a) and b) respectively.*

After the sample preparation, it was installed into the sample holder of the home-made setup for electrical conductivity/Seebeck coefficient studies [42], as shown in figure 2.3 b), and then put to the furnace. The measurement was performed in 10% $H_2$ + 90% $N_2$ atmosphere to simulate the fuel cell mode, in the temperature range from room temperature to 700 °C, both on heating and cooling in stepwise and continuous modes, depending on the sample behaviour.

After the electrical conductivity tests the bar was analysed by XRD and SEM/EDS; the obtained results were compared to the XRD results for ceramics before electrical measurements.

## 2.5 High-temperature XRD studies.

### 2.5.1 $10^{-3}$ millibar vacuum atmosphere.

Possible phase transformations in molybdenum-containing ceramics on heating were studied by non-ambient XRD on heating for 0.8 NTO composition. Before the study, a preliminary test of the reactivity between 0.8 NTO powder with Pt foil at 750 °C (100 °C higher than the highest temperature for the non-ambient XRD), performed in 10% $H_2$ + 90% $N_2$ atmosphere, in order to avoid possible damage to the equipment due contamination of Ni and Mo of the sample into the Pt coil of the heating system by intermetallic formation. The selected temperatures to perform XRD analysis corresponded to 150, 250, 350, 450, 550 and 650 °C. At 450, 550 and 650 °C two XRD scans at each temperature were taken: one after 15 min after reaching the corresponding temperature and another after 1 h of dwell. At lower temperatures, only one XRD scan was performed per temperature after 15 min of stabilization. The corresponding time-temperature profile is shown in figure 2.4. The measurements were performed in a $10^{-3}$ millibar vacuum atmosphere that corresponds to the oxygen pressure of $2\times10^{-7}$ atm. The heating rate between steps was 3 °C/min, while the cooling was 60 °C/min.

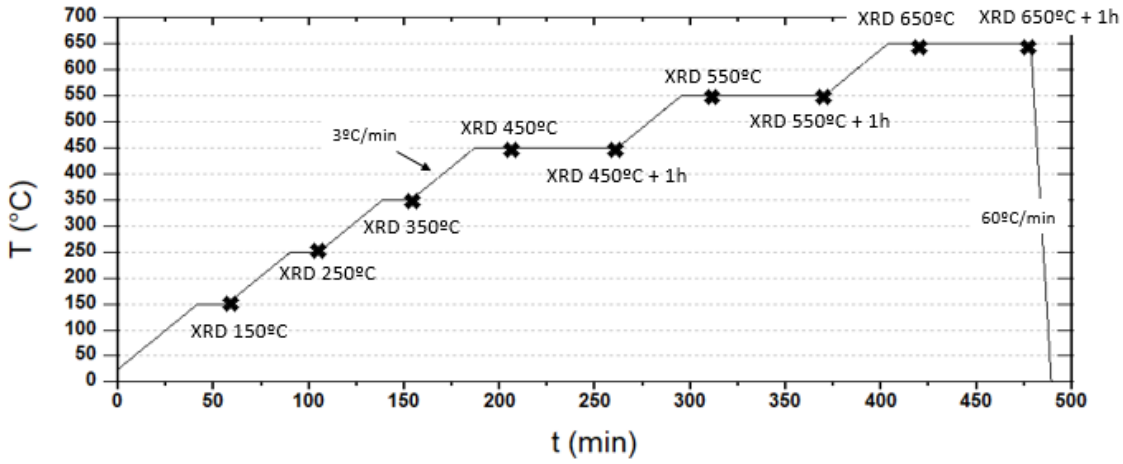


*Figure 2.4. Time-temperature profile of high-temperature XRD studies, the crosses indicate the XRD scans.*

### 2.5.2 **10% $H_2$ + 90% $N_2$** atmosphere.

Also, the phases composition transformations were studied in 10% $H_2$ + 90% $N_2$ atmosphere. For that the ceramic of 0.8NTO composition was grounded, to increase their surface area, with ethylene alcohol and dried, followed by the thermal treatment at 650 °C during 5h with 7 °C/min as the heating and cooling rate in the 10% $H_2$ + 90% $N_2$ atmosphere. After the thermal treatment the powder was analysed by XRD, and their result was compared with the initial one of the 0.8NTO composition ceramic.

## 2.6 Calculation of Ellingham diagram to estimate the stability of Magneli phases in 10% $H_2$ + 90% $N_2$ atmosphere.

The oxygen pressure equilibrium between consecutive Magneli phases was calculated using the thermodynamic data present in the literature [43], in the range of 400 °C to 1500 °C. The reactions considered for the calculation were the oxidation between sequential Magneli phases ($Ti_5O_9$ → $Ti_6O_{11}$ → $Ti_7O_{13}$ → $Ti_8O_{15}$ → $Ti_9O_{17}$ → $Ti_{10}O_{19}$ → $Ti_{20}O_{39}$ → $TiO_2$).

The 10% $H_2$ + 90% $N_2$ atmosphere, contains a fraction of water, shifting the water splitting equilibrium in which the $O_2$ can be release. The oxygen pressure thus depends on the reaction equilibrium, consequently from the temperature and the initial ratio between $p(H_2O)$ ⁄$p(H_2)$. Although the furnace used had a YSZ-based oxygen sensor, the temperature dependence of the oxygen pressure of furnace chamber must be re-calculated, since the oxygen sensor is located outside the furnace chamber, at a constant temperature of 850 °C. The oxygen pressure calculation was made using the eq. 2.2), where the initial ratio of $p(H_2O) / p(H_2)$ was estimated based on the eq. 2.3), and the sensor temperature of 850 °C.

$$\log P\ O_2 = \frac{\Delta G_r}{2.30RT} + 2\log\left(\frac{P\ H_2O}{P\ H_2}\right) \quad \text{eq. 2.2)}$$

$$\log\left(\frac{P\ H_2O}{P\ H_2}\right) = \frac{\log P\ O_2 - \frac{\Delta G_r}{2.30RT}}{2} \quad \text{eq. 2.3)}$$

## 2.7 Electrochemical characterization in alkaline medium.

In addition to structural and electrical characterization relevant for SOFC/SOEC applications, the prepared compositions were also preliminary tested as potential electrodes for hydrogen evolution for alkaline water electrolysis, and their behaviour on redox cycling was tested. Corresponding working electrodes were prepared in the form of pellets, more details on the electrode configuration and preparation can be found elsewhere [44]. Before electrochemical tests, the samples were polished until a thickness between 1.5 – 3.0 mm and a geometrical area of around ~ 0.7 $cm^2$, washed with distilled water and ethanol, and dried in the oven. Silver paste (Agar Scientific) was used to glue Ni-foil, acting as a current collector, to the samples and provide reliable electrical contact. The area of Ni supports, which is not in the contact with the sample and exposed to the electrolyte was painted with isolating lacquer (Lacomit Varnish, Agar Scientific) to avoid electrochemical contribution to the electrode processes. The whole face of the sample, connected to Ni support and containing silver paste, was also covered with the lacquer, together with lateral sides of the pellet. Thus, only one face of the pellet was exposed to the electrochemical reaction. The corresponding arrangement is shown in figure 2.5.

*Figure 2.5. Working electrode for electrochemical characterization.*

Electrochemical studies were performed at 90 °C, with an Autolab potentiostat (PGSTAT 20) connected to the electrochemical cell in a teflon reactor. A Pt wire was used as a counter electrode (CE) and Hg|HgO|NaOH (1 M) (+0.098 V versus saturated hydrogen electrode) as a reference electrode filled with NaOH (6 M), connected by a Luggin capillary to the electrolyte. The Luggin capillary must be placed in between the counter electrode with the working electrode as shown in figure 2.6.a). The figure 2.6.b) is a picture of the system with the heating system, showing the connections between the electrodes of the reactor with the potentiostat.

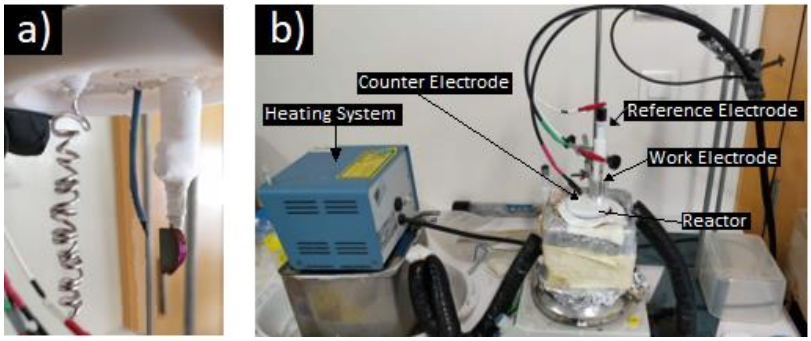


*Figure 2.6. a) Electrodes inside of the reactor and b) the whole system used for electrochemical analysis.*

The electrochemical study of the materials started with the initial characterization by electrochemical impedance spectroscopy (EIS), followed by cycling voltammetry. After one performed amperometry with cathodic polarization followed by the cycling voltammetry, to assure that the cycling voltammetry was performed on the most reduced surface as possible.

Next, the electrode was tested in redox cycling condition. Those started initially as anode, and the evolution was studied during 4 cycles of amperometry with anodic polarization intercalated with EIS, at the end of those cycles, cycling voltammetry was performed. After, the electrode worked as cathode, the evolution was characterized by 4 steps of amperometry with cathodic polarization intercalated with EIS, followed by cycling voltammetry.

Finally, another redox cycle was tested, in which the electrode started as the anode, by amperometry with anodic polarization, followed by EIS and cycling voltammetry, after the electrode worked again as cathode, by the amperometry with cathodic polarization followed by cycling voltammetry.

The parameters of electrochemical tests are listed in table 2.1.

*Table 2.1. Electrochemical study sequence, of the redox cycling, with the test's parameters detailed.*

| Electrode as: | Test sequence | Description |
|---|---|---|
| **Initial characterization** | Initial Impedance | Scan Range: [10000 to 0.1] Hz; Amplitude: 50 mV |
| | Initial Cycling voltammetry | Scan rate: 100mV/s; Range [-1.3→ +0.5→ -1.3] V; 3 cycle |
| | | Scan rate: 30mV/s; Range [-1.3→ +0.5→ -1.3] V; 3 cycle |
| | | Scan rate: 10mV/s; Range [-1.3→ +0.5→ -1.3] V; 3 cycle |
| | Cycling voltammetry after cathodic amperometry | 1 ° Amp: 15 min of cathodic pol. (-1.3V); 2 ° CV: Scan rate: 100mV/s; Range [-1.3→ +0.5→ -1.3] V; 3 cycle |
| | | 1 ° Amp: 15 min of cathodic pol. (-1.3V); 2 ° CV: Scan rate: 30mV/s; Range [-1.3→ +0.5→ -1.3] V; 3 cycle |
| | | 1 ° Amp: 15 min of cathodic pol. (-1.3V); 2 ° CV: Scan rate: 10mV/s; Range [-1.3→ +0.5→ -1.3] V; 3 cycle |
| **Anode** | Anodic amperometry (+0.5V) before impedance | 1 ° Amp:15 min anodic pol. (+0.5 V): 2 ° Impedance[1] |
| | | 1 ° Amp:15 min anodic pol. (+0.5 V); 2 ° Impedance[1] |
| | | 1 ° Amp:15 min anodic pol. (+0.5 V); 2 ° Impedance[1] |
| | | 1 ° Amp:15 min anodic pol. (+0.5 V); 2 ° Impedance[1] |
| | Cycling voltammetry | Scan rate: 100mV/s, Range [+0.5→ -1.3→ +0.5] V, 3 cycle |
| | | Scan rate: 30mV/s, Range [[+0.5→ -1.3→ +0.5] V, 3 cycle |
| | | Scan rate: 10mV/s, Range [+0.5→ -1.3→ +0.5] V, 3 cycle |
| **Cathode** | Cathodic polarization (-1.3V) before impedance | 1 ° Amp:15 min cathodic pol. (-1.3 V); 2 ° Impedance[1] |
| | | 1 ° Amp:15 min cathodic pol. (-1.3 V); 2 ° Impedance[1] |
| | | 1 ° Amp:15 min anodic pol. (-1.3 V); 2 ° Impedance[1] |
| | | 1 ° Amp:15 min anodic pol. (-1.3 V); 2 ° Impedance[1] |
| | Cycling voltammetry | Scan rate: 100mV/s, Range [-1.3→ +0.5→ -1.3] V, 3 cycle |
| | | Scan rate: 30mV/s, Range [-1.3→ +0.5→ -1.3] V, 3 cycle |
| | | Scan rate: 10mV/s, Range [-1.3→ +0.5→ -1.3] V, 3 cycle |
| **Anode** | Anodic amperometry (+0.5 V) | Amp: 1h, (+0.5V) |
| | Impedance | Scan Range: [10000 to 0.1] Hz; Amplitude: 50 mV |
| | Cycling voltammetry | Scan rate: 100mV/s, Range [+0.5→ -1.3→ +0.5] V, 3 cycle |
| | | Scan rate: 30mV/s, Range [+0.5→ -1.3→ +0.5] V, 3 cycle |
| | | Scan rate: 10mV/s, Range [+0.5→ -1.3→ +0.5] V, 3 cycle |
| **Cathode** | Cathodic polarization (-1.3) | Amp: 1 h; (-1.3V) |
| | impedance | Scan Range: [10000 to 0.1] Hz; Amplitude: 50 mV |
| | Cycling voltammetry | Scan rate: 100mV/s, Range [-1.3→ +0.5→ -1.3] V, 3 cycle |
| | | Scan rate: 30mV/s, Range [-1.3→ +0.5→ -1.3] V, 3 cycle |
| | | Scan rate: 10mV/s, Range [-1.3→ +0.5→ -1.3] V, 3 cycle |

[1] Scan Range: [10000 to 0.1] Hz; Amplitude: 50 mV

## 2.8 Pourbaix diagram calculation.

The Ni, Mo and Ti with Magneli phases Pourbaix diagrams were drawn, in which the temperature considered was 25 °C.

For Ni and Mo, the diagram was only redrawn from the data present in literature [45]. While for the Ti and Magneli phases, the Pourbaix diagram of Ti and its oxides was extended from its original version [45] to include some expected Magnelli phases, the potentials for these ones were estimated based on available information on free energies of formation of expected Magnelli phases [40], including oxidative dissolution of different oxides (eq. 2.4) and redox reactions between two oxide pairs (eq. 2.5):

$$Ti_nO_{2n-1} + 2(2n-1)H^+ + 2(n-1)e^- \rightleftharpoons nTi^{2+} + (2n-1)H_2O \qquad \text{eq. 2.4)}$$

$$mTi_nO_{2n-1} + 2(n-m)H^+ + 2(n-m)e^- \rightleftharpoons nTi_mO_{2m-1} + (n-m)H_2O \qquad \text{eq. 2.5)}$$

The corresponding electrode potentials for oxidative dissolution and their dependence on pH and or activity of soluble species can be predicted by Nernst law, yielding, as shown by eq. 2.6):

$$E = -\frac{n\left\{\Delta G_f^o\right\}_{Ti^{2+}} + n\left\{\Delta G_f^o\right\}_{H_2O} - \left\{\Delta G_f^o\right\}_{Ti_nO_{2n-1}}}{2(n-1)F} - \frac{2.30(2n-1)RT}{(n-1)F}pH - \frac{2.30nRT}{2(n-1)F}log[Ti^{2+}] \qquad \text{eq. 2.6)}$$

Similarly, the eq. 2.7) represents the redox reactions between two oxide pairs:

$$E = -\frac{n\left\{\Delta G_f^o\right\}_{Ti_mO_{2m-1}} + (n-m)\left\{\Delta G_f^o\right\}_{H_2O} - m\left\{\Delta G_f^o\right\}_{Ti_nO_{2n-1}}}{2(n-1)F} - \frac{2.30RT}{F}pH \qquad \text{eq. 2.7)}$$

Based on these calculations one expects the following sequence of Magnelli phases in alkaline aqueous solutions, with increasing potential:

$$Ti < Ti_3O_2 < TiO < Ti_2O_3 < Ti_5O_9 < Ti_6O_{11} < Ti_8O_{15} < Ti_9O_{17} < Ti_{20}O_{39} < TiO_2$$

Table 2.2, describes the different reactions considered as their conditions of equilibrium, represented on the Pourbaix diagram.

*Table 2.2. Free energy of formation and representative reactions between oxides or metal and ionic species in aqueous solutions.*

| Species | $\Delta G_f^o$ (kJ/mol) | Reaction | Condition of equilibrium |
|---|---|---|---|
| $Ti^{2+}$ | -75.10 | | |
| $Ti_3O_2$ | -1028 | $3Ti^{2+} + 2H_2O + 2e^- = 4H^+ + Ti_3O_2$ | $E= -2.011+0.118pH+0.089\log[Ti^{2+}]$ |
| $TiO$ | -513 | $TiO+2H^+ = Ti^{2+} + H_2O$ | $pH= 3.34-0.5\log[Ti^{2+}]$ |
| $Ti_2O_3$ | -1434 | $2e^- + 6H^+ + Ti_2O_3 = 2Ti^{2+} + 3H_2O$ | $E= -0.491-0.177pH-0.059\log[Ti^{2+}]$ |
| $Ti_3O_5$ | -2317 | $4e^- + 10H^+ + Ti_3O_5 = 3Ti^{2+} + 5H_2O$ | $E= -0.491-0.148pH-0.044\log[Ti^{2+}]$ |
| $Ti_4O_7$ | -3213 | $6e^- + 14H^+ + Ti_4O_7 = 4Ti^{2+} + 7H_2O$ | $E= -0.513-0.138pH-0.039\log[Ti^{2+}]$ |
| $Ti_5O_9$ | -4114 | $8e^- + 18H^+ + Ti_5O_9 = 5Ti^{2+} + 9H_2O$ | $E= -0.531-0.133pH-0.037\log[Ti^{2+}]$ |
| $Ti_6O_{11}$ | -5005 | $10e^- + 22H^+ + Ti_6O_{11} = 6Ti^{2+} + 11H_2O$ | $E= -0.532-0.130pH-0.035\log[Ti^{2+}]$ |
| $Ti_7O_{13}$ | -5895 | $12e^- + 26H^+ + Ti_7O_{13} = 7Ti^{2+} + 13H_2O$ | $E= -0.531-0.128pH-0.034\log[Ti^{2+}]$ |
| $Ti_8O_{15}$ | -6785 | $14e^- + 30H^+ + Ti_8O_{15} = 8Ti^{2+} + 15H_2O$ | $E= -0.530-0.127pH-0.034\log[Ti^{2+}]$ |
| $Ti_9O_{17}$ | -7675 | $16e^- + 34H^+ + Ti_9O_{17} = 9Ti^{2+} + 17H_2O$ | $E= -0.530-0.126pH-0.033\log[Ti^{2+}]$ |
| $Ti_{10}O_{19}$ | -8564 | $18e^- + 38H^+ + Ti_{10}O_{19} = 10Ti^{2+} + 19H_2O$ | $E= -0.529-0.125pH-0.033\log[Ti^{2+}]$ |
| $Ti_{20}O_{39}$ | -17460 | $38e^- + 78H^+ + Ti_{20}O_{39} = 20Ti^{2+} + 39H_2O$ | $E= -0.527-0.121pH-0.031\log[Ti^{2+}]$ |
| $TiO_2$ | -889 | $2e^- + 4H^+ + TiO_2 = Ti^{2+} + 2H_2O$ | $E= -0.524-0.118pH-0.030\log[Ti^{2+}]$ |
| $H_2O$ | -237 | | |
| $Ti$ | 0 | | |
| $H^+$ | 0 | | |

## 2.9 Open porosity estimation.

The estimation was done based on the Archimedes' method. For that, the sample were weighted at different stages. Firstly, the sample dried in the oven at 60 °C during one night. Next, the sample were boiled in distilled water for 15 min followed by application of vacuum, and the wet mass of the sample was measured. Finally, one measured the mass of the system immersed in water without and with the sample to obtain the apparent mass of the sample, when immersed in water.

After, the open porosity was calculated by the eq. 2.8) [46], where $wt_1$, $wt_2$, and $wt_3$ represents respectively the dry mass, wet mass and apparent mass of the samples:

$$x_o = \frac{wt_2 - wt_1}{wt_2 - wt_3} \qquad \text{eq. 2.8)}$$

# 3 Results and discussion.

## 3.1 Optimization of the powder processing routes.

The application of Pechini method for preparation of nanosized powders with a suitable phase composition implies optimization of many parameters, including the metal-to-citrate molar ratio, selection of initial chemicals, conditions of dissolution and mixing, and gel drying. Those first parameters were selected based on the existing experience of the supervisor´s group, and the conditions for thermal post-treatments were optimized to attain the objectives of the work.

The treatment by Pechini method may result in a mixture of oxides with carbonates, thus, it is necessary to calcinate them to obtain the target materials. For that, the thermal cycle had to be optimized to obtain the required phases: $NiTiO_3$ in NTO powder composition and a mixture of $NiTiO_3$ with $MoO_3$ for 0.9NTO and 0.8NTO powders, respectively. The optimization was performed using 5 g of NTO powder composition and different calcination routes to ensure the formation of the $NiTiO_3$ phase.

The diffraction pattern of the powders before calcination and after three different heating cycles are shown in figure 3.1. Already in the case of the powder after synthesis by Pechini method, assigned by “Before calcination” in the figure 3.1, the diffraction pattern showed that the phase with higher quantity was the desired $NiTiO_3$. However, the secondary phases as $TiO_2$ (rutile and anatase) and NiO were also detected. The presence of carbon was not revealed by the diffraction pattern, however, it was perceived by the colour change on the powder between, before and after the calcination, from grey to yellow, respectively.

The first calcination attempted corresponded to 6 hours at 800 °C, with a heating and cooling rate of 3 °C/min, and corresponding diffraction pattern is designated by” H.R: 3 °C/min” on figure 3.1. In this case, the quantity of $NiTiO_3$ phase was reduced as compared to the powder before calcination, while the amount of secondary phases as rutile and NiO was increased. Surprisingly, this thermal treatment procedure also resulted in formation of metallic Ni. This indicates that the selected heating rate was apparently too high, allowing reaching the temperatures, where nickel oxide can be reduced by carbon at noticeable rate, before burn-out of carbon-rich phase. This assumption was considered for scheduling further thermal treatments.

The results for thermal treatment at the same top temperature (800 °C) and dwell time (6 h), but essentially lower heating rate of 1 °C/min are designated as “H. R:1 °C/min; 5 g” (figure 3.1). In this case the powder is monophasic, with the desired $NiTiO_3$ ilmenite-type structure.

Since further characterization studies required larger amounts of powder, and additional heat treatment attempt was performed for 15 g of the same powder, taking into account that oxygen diffusion to the powder volume and carbon burn-out instead of NiO reduction may be impeded by larger powder quantities. So, to assure that the release of carbon was complete before the sample reaches the temperature at which carbon starts to act as a reducing agent for NiO, the thermal cycle was changed: from the room temperature to 300 °C the heating rate was 5 °C/min to reduce the cycle duration, from 300 °C to 600 °C/min the heating rate was 1 °C/min, followed by the first annealing for 6 hours at 600 °C, further heating up to 800 °C at 1 °C/min and the second annealing step at 800 °C for 6 hours. After, the powder was cooled down to room temperature at 1 °C/min. The figure 3.2 represents the thermal cycle for the powder calcination. The diffraction pattern for the resulting is also shown in figure 3.1, designated by “H.R:1 °C/min; 15 g”. Similar to

the case of "H.R:1 ° C/min; 5 g" the powder was monophasic indicating that the carbon release was complete before it could act as a reducing agent for nickel oxide.

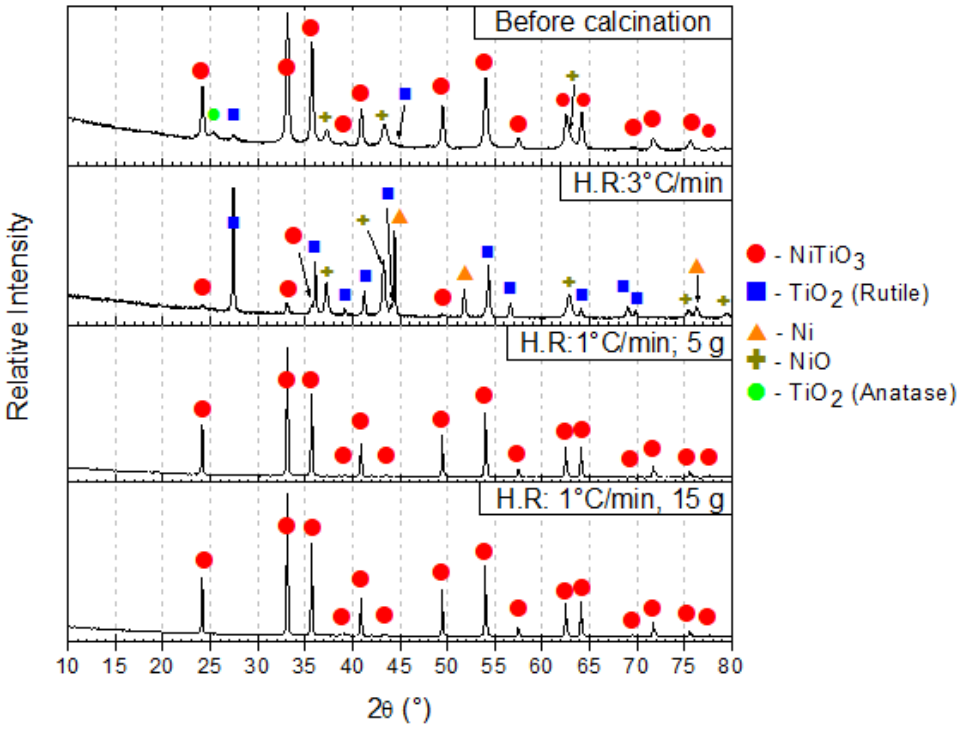


*Figure 3.1. Diffraction patterns for the powders obtained using different thermal cycles used to calcinate the precursor of NTO composition, after synthesis by Pechini method. "Before calcination" corresponds to the powder after synthesis by Pechini method without calcination, "H.R:3 °C/min" to the calcination at 800 °C during 6h with heating rate of 3 °C/min, "H.R:1 °C/min; 5 g" to the calcination at 800 °C during 6 h with heating rate of 1 °C/min, and finally the "H.R:1ºC/min, 15g" corresponds to the longest thermal cycle described in figure 3.2 .*

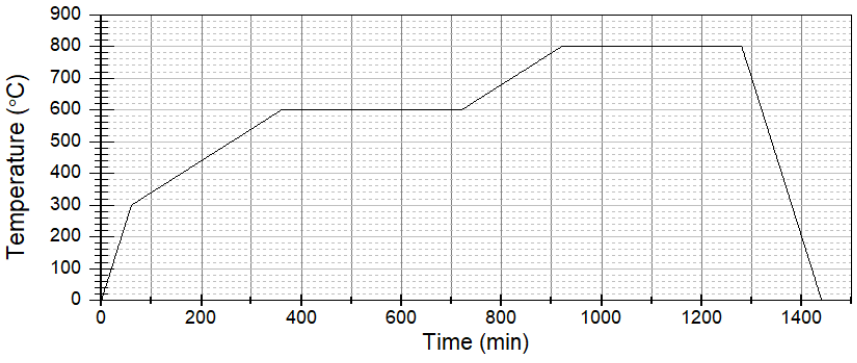


*Figure 3.2. Thermal cycle used to calcinate 15 g of each composition.*

Following the obtained results, showing the heat treatment conditions which result in monophasic $NiTiO_3$ powder, the same calcination procedure was applied for 15 g of the other Mo-containing composition, followed by XRD analyses. Corresponding diffraction patterns are shown in figure 3.3. The results showed the formation of $NiTiO_3$, $NiMoO_4$ and $TiO_2$ phases, while the appearance of several minor non-identified peaks was also observed. It is likely that those minor impurities contain molybdenum, as their intensity increases (e.g., the peak at 2θ ~ 27.5 °) with increasing the molybdenum content.

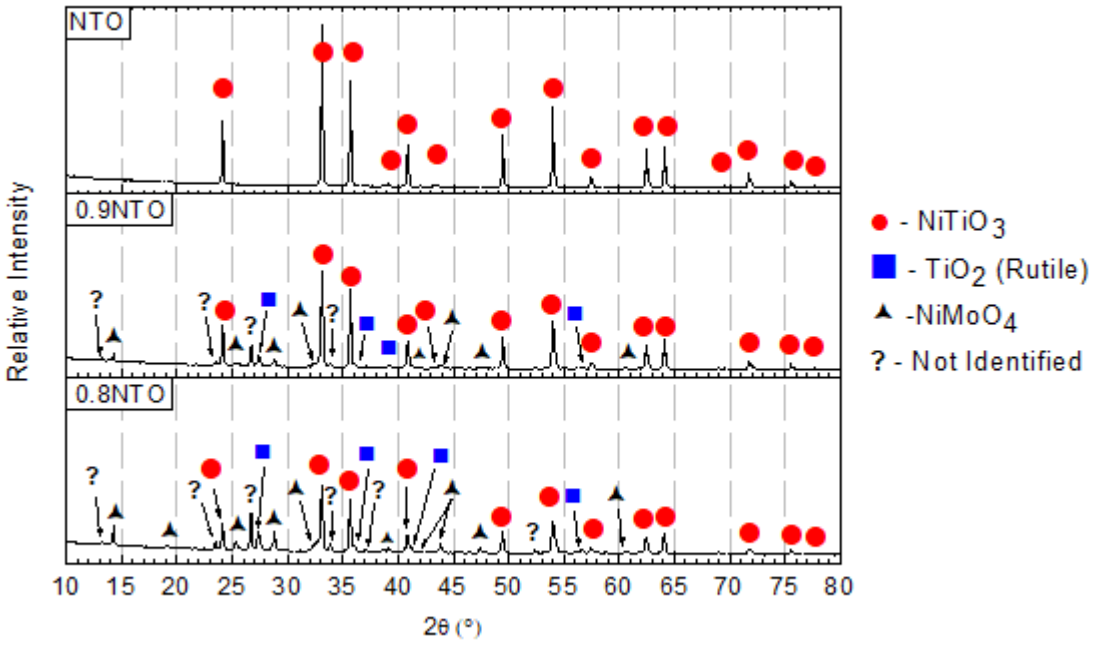


*Figure 3.3. Diffraction pattern of each composition, when was produced 15 g of those.*

The microstructure of the produced powders was analysed by SEM and EDS, as represented by figure 3.4. The results confirm the formation of nanosized powder for NTO composition figure 3.4.a), with a relatively high degree of agglomeration. Similar agglomeration of the nanopowders was revealed for 0.9NTO and 0.8NTO figure 3.4.b), and figure 3.4.c), along with the presence of larger elongated grains of the $NiMoO_4$ phase, as suggested by EDS mapping results (figure 4d)-g)). It also appears that the presence of molybdenum is favourable for the formation of smaller $NiTiO_3$ particles, however, the related mechanism is not yet clear.

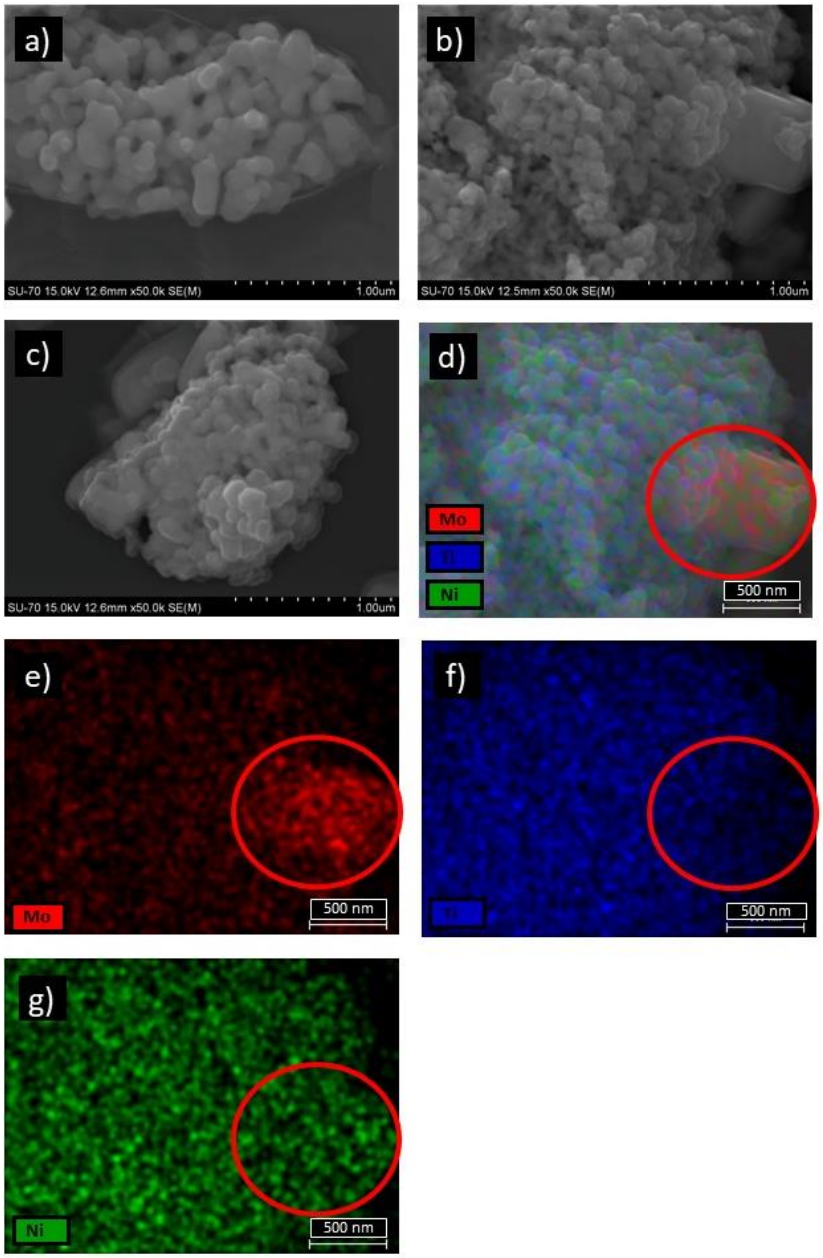


*Figure 3.4. Microstructural analysis of the powders by SEM at magnification of 50K, a) NTO powder, b) 0.9NTO powder, and c) 0.8NTO powder. Elemental EDS mapping results for the microstructure are shown on b): d) the mapping of all elements, and e) f) and g) of each element, Mo, Ti and Ni respectively.*

## 3.2 Ceramics processing.

Relevant electrical characterization of the materials suitable for the electrodes of reversible solid oxide fuel cell requires the preparation of dense or nearly-dense ceramics. Thus, several steps for the optimization of ceramics processing were also done.

The molybdenum oxides are known to be volatile under oxidizing conditions [47] [48]. In order to test the phase composition and possibilities for partial retaining of molybdenum in air, small ceramic pellets of NTO and 0.9NTO composition were sintered at 1200 °C, while the 0.8NTO composition was sintered at 1300 °C. The quantities were quite small in order to avoid possible furnace contamination. After sintering, the phase composition was analysed by the XRD diffraction, the results are shown in the figure 3.5.

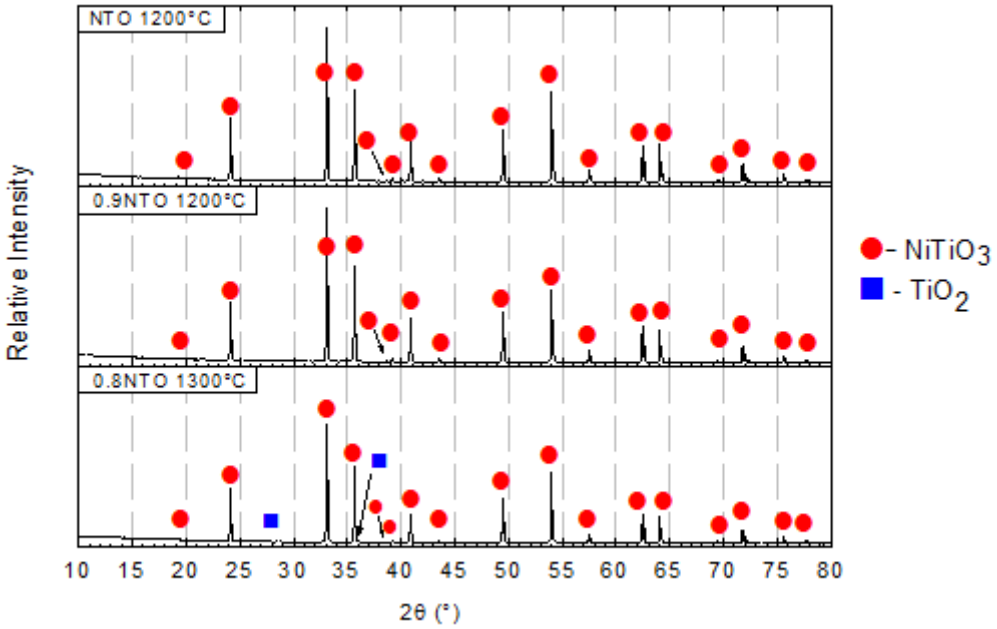


*Figure 3.5. Diffraction pattern of the samples sintered in air for 5 h.*

Only $NiTiO_3$ for all tested compositions and a minor amount of $TiO_2$ phase for 0.8NTO were observed. This suggests that the molybdenum is volatilized, or is incorporated in the crystal lattice of the $NiTiO_3$ phase. To check the latter assumption, the unit cell parameters of the rhombohedral $NiTiO_3$ lattice were calculated for each composition and listed in Table 3.1.

*Table 3.1. Unit cell parameter of the NiTiO3-based phase in the ceramics sintered in air atmosphere.*

| Composition | a, b | c | $Chi^2$ |
|---|---|---|---|
| **NTO** | 5.0305 | 13.7871 | 13.5 |
| **0.9NTO** | 5.0314 | 13.7894 | 12.8 |
| **0.8 NTO** | 5.0315 | 13.7908 | 14.6 |

Although the obtained lattice parameters show a small tendency to increase on adding molybdenum, this variation is quite minor. A small fraction of molybdenum apparently still can be retained by $NiTiO_3$ lattice even under oxidizing conditions, this is also indirectly evidenced by a minor segregation of $TiO_2$, observed for the 0.8NTO composition. However, the major part of molybdenum oxide seems to be volatilized. These results indicate that the processing or direct use of the selected compositions in air at elevated temperatures should be avoided. Instead, one can assume the applications and processing conditions, where oxygen partial pressure may vary from highly reducing to nearly inert.

First attempt to sinter NTO and 0.9NTO ceramics in the conditions which prevent molybdenum losses was performed in 10% $H_2$ +90% $N_2$ atmosphere, at 1200 °C for 5 h using 3 °C/min the heating and cooling rates. Figure 3.6 shows corresponding diffraction patterns, indicating that $NiTiO_3$ was reduced to metallic Ni and $Ti_6O_{11}$ Magnéli phase, the composition also contains rutile. The separate attribution of the peaks to $Ti_6O_{11}$ and rutile was complicated by their overlapping. However, during the identification, one took into account the small deviation of the peaks angle between the diffraction patterns and the ratio of intensity between peaks of the same phase. Also, a shift to the lower 2θ angle was observed for the Ni metallic peaks in the 0.9NTO sample when compared with the NTO sample. This can be explained by the increase of the cell parameters of the nickel crystal lattice by intercalation of Mo, yielding to a solid solution.

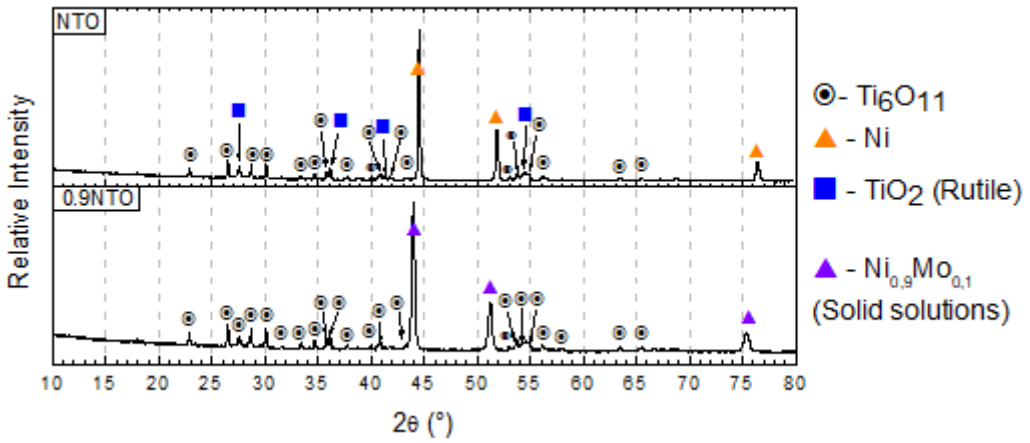


*Figure 3.6. Diffraction patterns of NTO and 0.9NTO compositions sintered at 1200ºC, for 5h in 10% $H_2$ + 90% $N_2$ atmosphere.*

The presence of rutile residues in the case of NTO composition suggests that the selected sintering conditions still result in fully oxidized forms of titania. Thus, another pellet was sintered at a higher reducing temperature of 1300 °C, in reducing atmosphere, using the same dwell time and heating/cooling rates. The formation of dense and high-quality ceramics was observed. Further analysis of the relevant properties was conducted for ceramics produced under these conditions.

The data corresponding to the density measurement is given in Table 3.2. The density increases on increasing heavier molybdenum content. As an example, Table 3.3 lists the density of the phases, characterised on the respective powder diffraction file (PDF), which might be present in the samples.

*Table 3.2. Density of the ceramic pellets sintered at 1300 °C during 5 h, in 10% $H_2$ + 90% $N_2$.*

| Sample | Density [$g/cm^3$] |
|---|---|
| **NTO** | 4.65 |
| **0.9NTO** | 5.05 |
| **0.8NTO** | 5.42 |

*Table 3.3. Density of metallic and ceramic phases expected to be present in the material.*

| Phases | Density [$g/cm^3$] |
|---|---|
| $MoNi_4$ | 9.42 |
| $Ni$ | 8.91 |
| $TiO_2$ | 4.2 |
| $Ti_6O_{11}$ | 4.3 |
| $Ti_8O_{15}$ | 4.28 |

Figure 3.7 shows the diffraction patterns after sintering at 1300 °C of the pellets, which were first isostatically pressed. The patterns show the presence of Magneli phases for 0.9 and 0.8NTO compositions, although in the case of 0.9NTO the Magneli phases $Ti_8O_{15}$ were more oxidized than the ones observed at lower temperature $Ti_6O_{11}$. At the same time, the results for NTO composition surprisingly show the presence of only rutile and metallic nickel. Since the sintering temperature was increased, the reduction was expected to be deeper; however, if one compares the diffraction patterns for the ceramics of NTO composition sintered at 1300 °C and at 1200 °C, the results appear to be contradictory to the expectations. To avoid errors associated with the furnace and/or gas atmosphere control malfunctioning, the sintering cycles were reproduced.

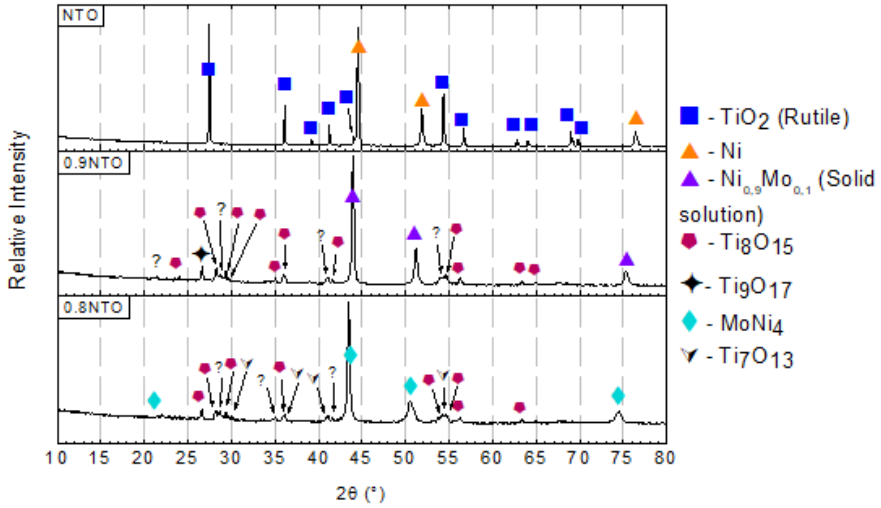


*Figure 3.7. Diffraction pattern of the composition sintering at 1300 °C for 5 h in 10% $H_2$ + 90% $N_2$ and were isostatically pressed.*

The diffraction pattern of the NTO sample sintered in the same conditions as a reproducibility experiment, presented in figure 3.8, shows the presence of rutile as in the previous case, thus confirming the reproducible results. Therefore, a possible explanation may include the effects of the powder processing conditions, namely, pressing procedure. The sample sintered at 1300 °C was isostatically pressed, while the sample sintered at 1200 °C was only uniaxially compacted. Isostatic pressing leads to much denser material, as compared to the uniaxial pressing. This diminishes the amount of porosity and voids, thus impeding the diffusion of gaseous reducing species. On the contrary, in the compositions with molybdenum, more voids were formed due to the reduction of the corresponding oxides to metallic form, providing sufficient diffusion pathways to reduce rutile to Magneli phases. This effect is well illustrated by the comparison of the phase composition for 0.9NTO: the sample, uniaxially pressed and sintered at 1200 °C, figure 3.6, shows the presence of more reduced $Ti_6O_{11}$ Magneli phase as compared the sample sintered at 1300 °C, where the formation of $Ti_8O_{15}$ and $Ti_9O_{17}$ was observed.

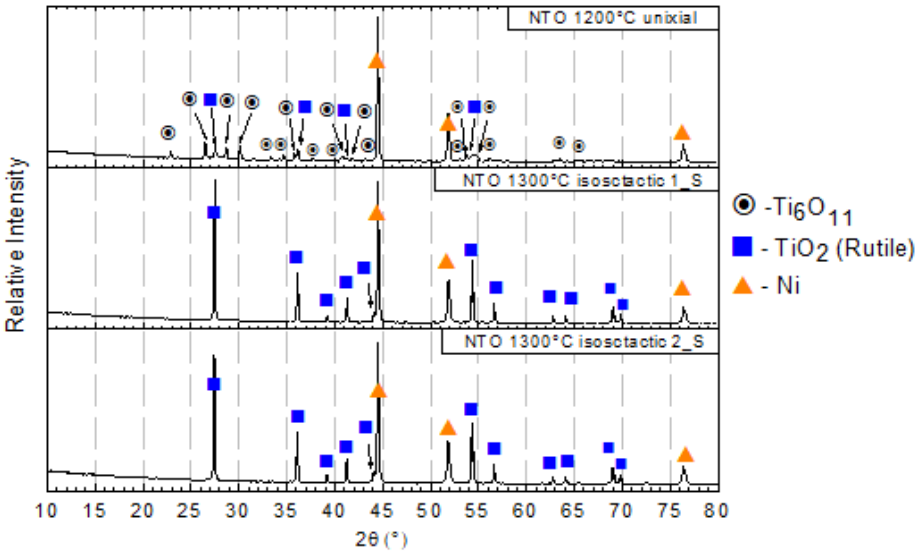


*Figure 3.8. Diffraction patterns of NTO composition sintered at 1200 °C for 5 h in 10% $H_2$ + 90%$N_2$ compacted only by uniaxial pressing, while the ones sintered at 1300 °C for 5 h in 10% $H_2$ + 90% $N_2$ were isostatically pressed.*

To verify the above discussion, the NTO ceramics was finally sintered at 1300 °C during 5 hours in the same reducing atmosphere, using only uniaxial pressing for the green compact preparation. The results, shown in figure 3.9 confirm the formation of reduced Magneli phases for the uniaxially-pressed samples.

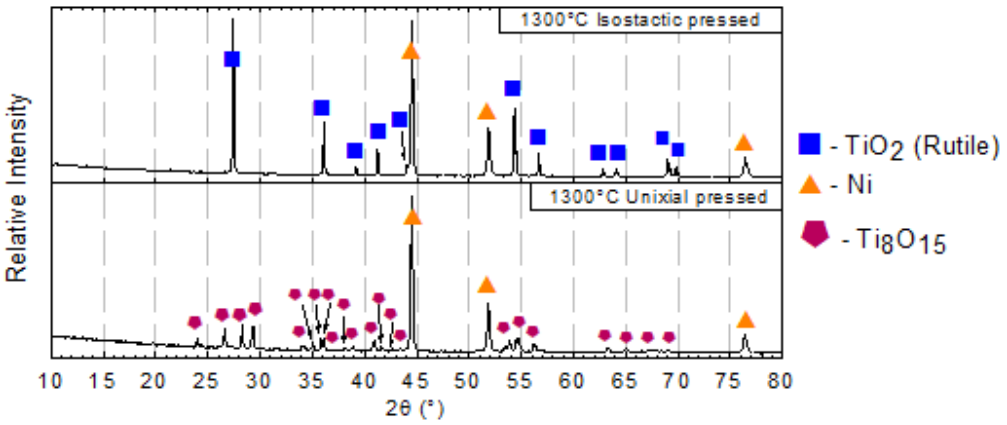


*Figure 3.9. Effect of pressing mode on diffraction pattern of NTO composition sintered at 1300 °C on 10% $H_2$ + 90% $N_2$ atmosphere.*

The density of the uniaxially-pressed NTO sintered at 1300 °C corresponded to ~4.00 g/cm$^3$, confirming lower densification than that attained for the isostatically-pressed NTO (4.65 g/cm$^3$), sintered at 1300 °C (Table 3.2).

From the microstructure analysis, through SEM and EDS presented in figure 3.10, one noticed that the ceramic of NTO composition, figure 3.10.a, is the one that shows higher porosity,

as expected by their density 4.00 g/cm$^3$ when compared with the other compositions, 0.9 NTO and 0.8NTO, respectively 5.05 and 5.42 g/cm$^3$.

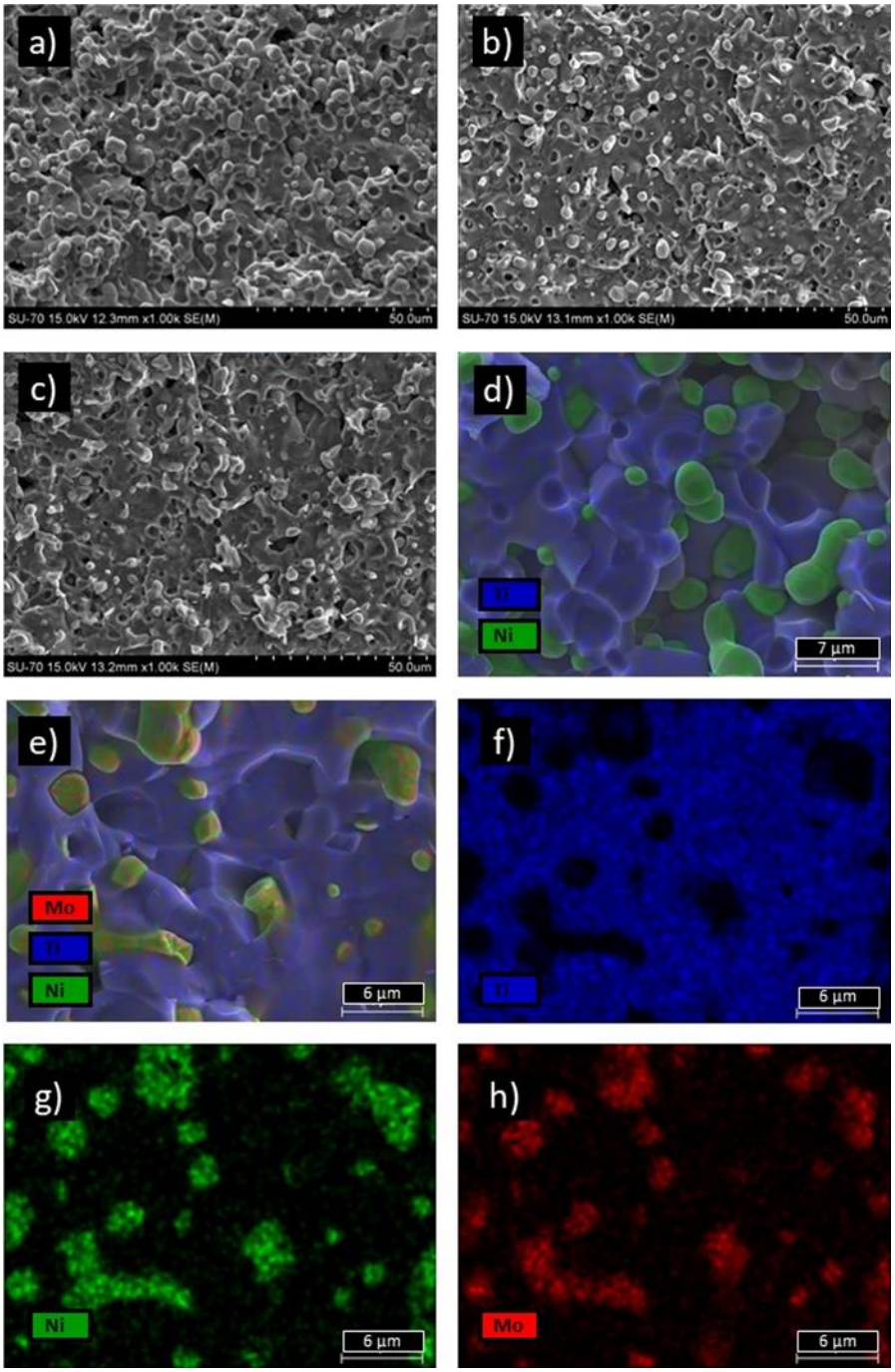


*Figure 3.10. Microstructural analysis of the ceramics by SEM at magnification of 1K, a) NTO, b) 0.9NTO, and 0.8NTO composition. Elemental EDS mapping, of all elements, for the NTO composition d), 0.8NTO composition e), and for each element, Ti, Ni and Mo; f), g) and h) respectively, for the 0.8NTO composition.*

For the NTO composition the structure analyses, figure 3.9 “1300 °C Uniaxial pressed” shows the presence of Ni and Magnelli phase, while their microstructure, figure 3.10.d), shows the Ni-rich precipitates on the Magnelli phases matrix, evidencing that during the sintering the Ni was

segregated from the $NiTiO_3$. In the case of the 0.8NTO composition the structure analyses, figure 3.7 "0.8NTO" reveals that the phase composition was Magneli phase and an intermetallic $MoNi_4$, and their microstructure analyses, figure 3.9. e-h) EDS mapping for all and each element Ti, Ni, and Mo respectively, figure 3.10.e), figure 3.10.f), figure 3.10.g) and figure 3.10.h) shows that Mo co-segregates with Ni, indicating the formation of an intermetallic of Ni with Mo, distributed on a titanium content matrix, and by the structural analysis the intermetallic was concluded to be $MoNi_4$, in a Magnelli phases matrix.

In general, the results show that the microstructural features may have a significant impact on the phase composition of ceramic NTO samples. Low densification is crucial for the reduction of $Ti^{4+}$ to Magneli phases, containing $Ti^{3+}$. The electrical conductivity of such samples is expected to be extremely sensitive to the extent of the reduction, while higher kinetic limitations of the reduction at lower temperatures, rather suitable for the operation of reversible SOFC, may further complicate the use of these materials as electrodes. At the same time, the presence of molybdenum is likely to improve the situation, by creating the internal porosity due to metal reduction and expected the higher catalytic activity of the intermetallic $MoNi_4$ phase [49].

## 3.3 Electrical conductivity and its dependence on heat treatment at intermediate temperatures.

The relevant samples set selected for the characterization of the electrical conductivity included NTO (uniaxially pressed), 0.9NTO and 0.8NTO (isostatically pressed) sintered at 1300 °C for 5 h. In this case, the samples are expected to possess a comparable level of reduction, which is, at the same time, appropriate to provide acceptable electrical conductivity values. Figure 3.11 represents the electrical conductivity in relation with time and temperature, in 10% $H_2$ + 90% $N_2$ atmosphere, for the NTO, 0.9NTO and 0.8NTO, a), b) and c) respectively. The initial values of the conductivity at low temperature are relatively high and correspond to ~200 S/cm for NTO, ~270 S/cm for 0.9NTO and ~500 S/cm for 0.8NTO, expectedly increasing on adding molybdenum. At 130 – 280 °C the variations of conductivity with temperature are quite moderate, with almost metallic-like behaviour in the case of 0.8NTO.

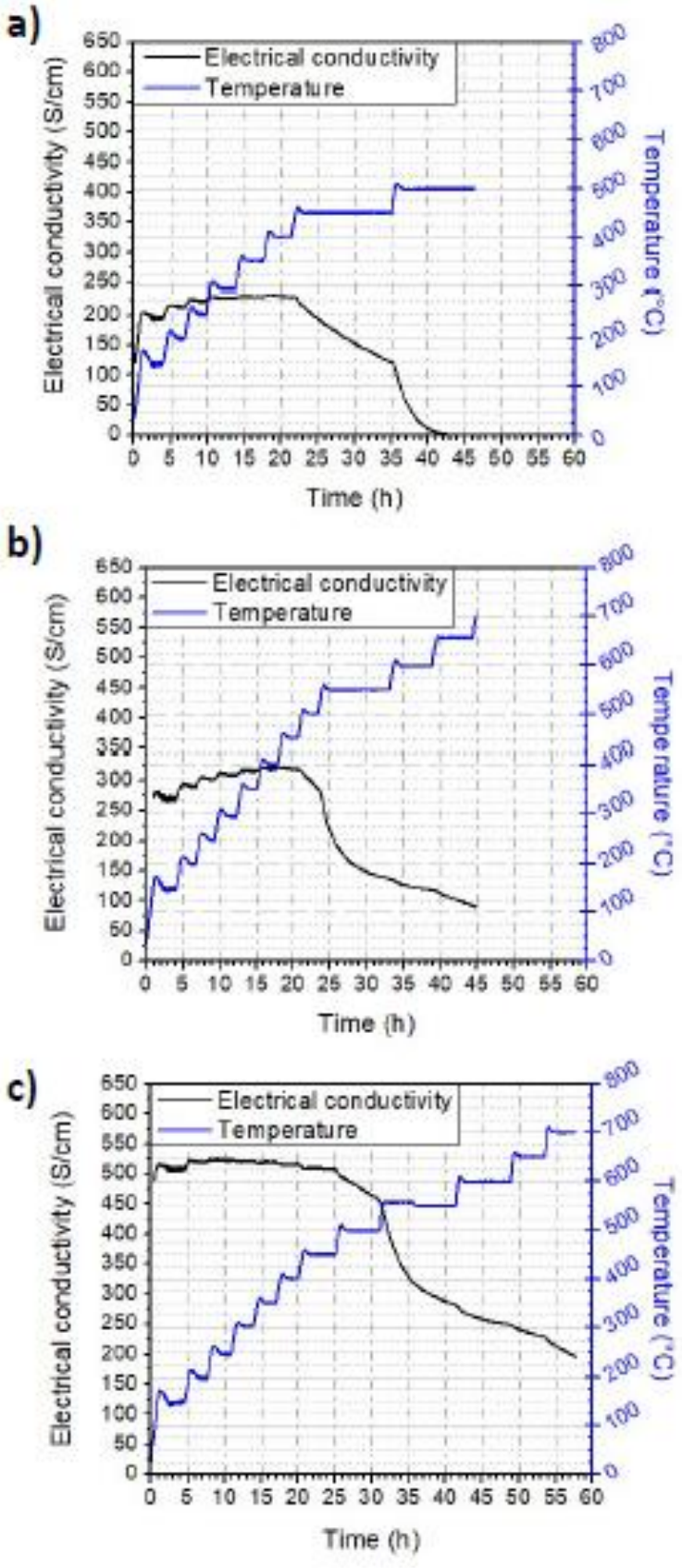


*Figure 3.11. Electrical conductivity vs time and temperature in 10% $H_2$ + 90% $N_2$ atmosphere for NTO (a); 0.9NTO (b) and 0.8NTO (c) respectively.*

The highest values of the electrical conductivity reached for each composition are listed in table 3.4. This dependence on temperature and time cannot be ascribed to metallic behaviour and reveals fast degradation mainly at T ≥ 450 °C. Further heating leads to the fast degradation of the electrical properties, associated with a large conductivity drop. In particular, the conductivity for NTO composition quickly dropped to values below 1 S/cm already after heating up to ~500 °C. It should be noticed that values >100 S/cm are often assumed as required for SOFC anodes, like in the case Ni-YSZ cermets [50]. Still, the conductivity drop was rather moderate in the case of molybdenum-containing samples. The rate of this degradation obviously depends on the heating profile, and more detailed studies are necessary to assess the kinetics of this process.

*Table 3.4. Highest electrical conductivity, with the corresponding temperature for each composition.*

| Composition | Highest electrical conductivity (S/cm) | Temperature ( °C) |
|---|---|---|
| **NTO** | 230 | 400 |
| **0.9NTO** | 320 | 460 |
| **0.8NTO** | 520 | 260 |

## 3.4 Post-mortem analysis after electrical measurements at intermediate temperatures

After the electrical conductivity measurements, the samples were analysed by XRD to check the phase transformations that could explain the observed degradation. Figure 3.12 shows the comparison between the diffraction patterns before with after electrical conductivity measurement for each composition. For all composition, the oxidation of Magneli phases to rutile was observed. Table 3.5 [51], shows the values of electronic conductivity for different Magneli phases and highlights that the conductivity is lower for more oxidised Magneli phases. Thus, even partial oxidation of one Magneli phase to another is expected to result in a noticeable conductivity drop. A surprising fact is that this oxidization takes place even during the electrical conductivity measurement in a highly reducing, 10% $H_2$ + 90% $N_2$ atmosphere, showing that the Magneli phases are very unstable. Apparently, the residual water vapour in the gas acts as a source of oxygen in this case.

*Table 3.5. Electronic conductivity of Magneli phases. [51]*

| Phase | Conductivity (S/cm) |
|---|---|
| **$Ti_5O_9$** | 631 |
| **$Ti_6O_{11}$** | 63 |
| **$Ti_8O_{15}$** | 25 |

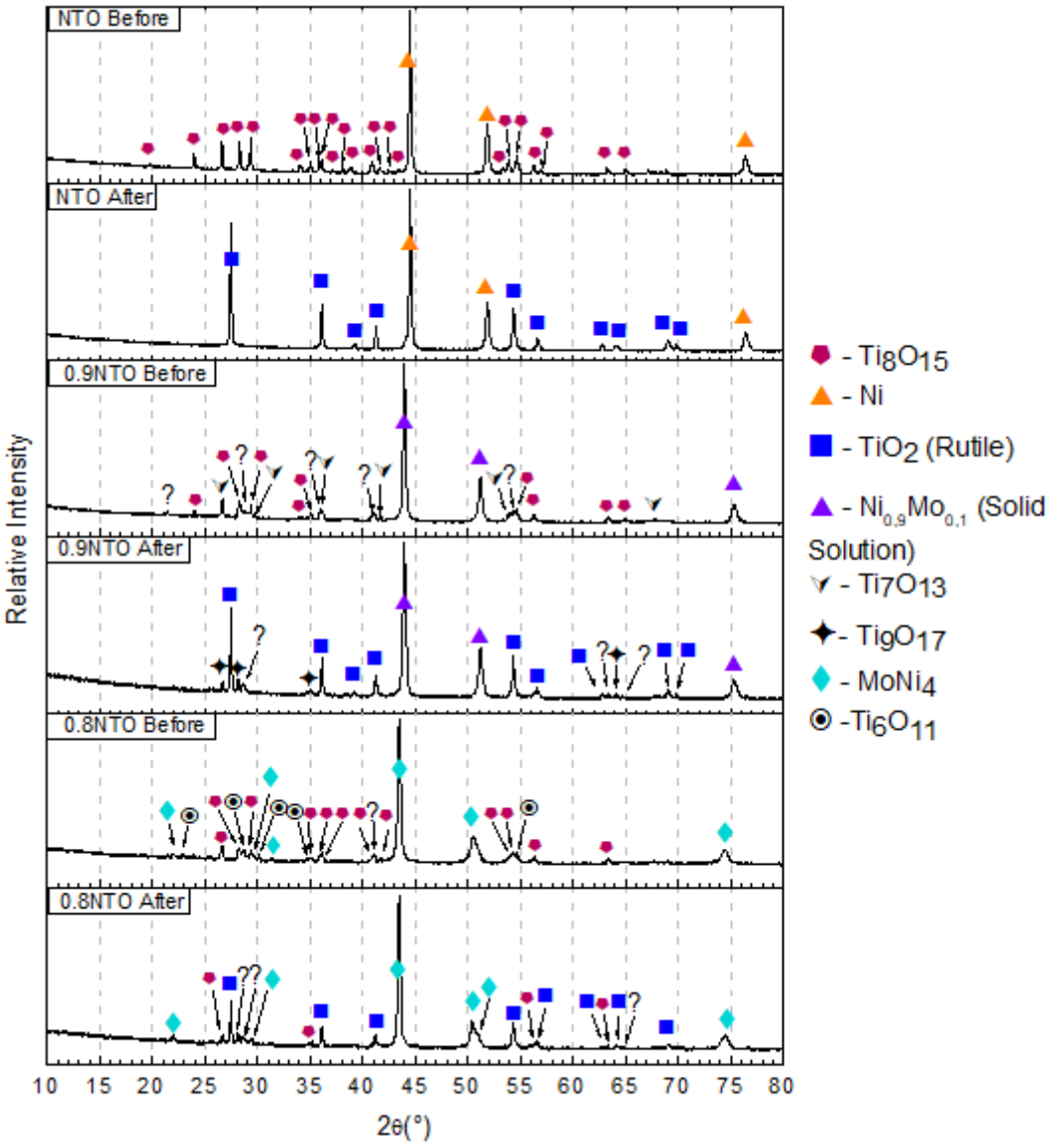


*Figure 3.12. Diffraction patterns for each composition before and after electrical conductivity measurement.*

It should be noticed that this oxidation during electrical measurements results in a complete transformation of the initial Magneli phases, presented in NTO sample, to rutile. On the contrary, although the rutile also appears in 0.8NTO samples, this samples still retain some fraction of the initial Magneli phases after the measurement. Thus, the ceramic matrix of the samples with molybdenum may still possess higher conductivity that in the case of NTO, explaining higher electrical conductivities of 0.9NTO and, especially, 0.8NTO.

Figure 3.13 represents the ceramic microstructures, before and after the electrical conductivity test of each composition, to explain the electrical conductivity degradation. The elemental mapping was not performed, since phase transformations from Magneli phases to rutile only imply small changes in oxygen stoichiometry, and these are hardly revealed by EDS. The

differences noted were the transformation on the matrix surface, from a smooth to irregular surface, present inside red circles. Also, this transformation was higher on the NTO composition, requiring a lower magnification, (i.e. 4K), to visualize than the other composition, (20K). This is coherent with the electrical degradation results, since the sample with higher electrical conductivity degradation (NTO composition) is the one with highest irregular surface of the matrix.

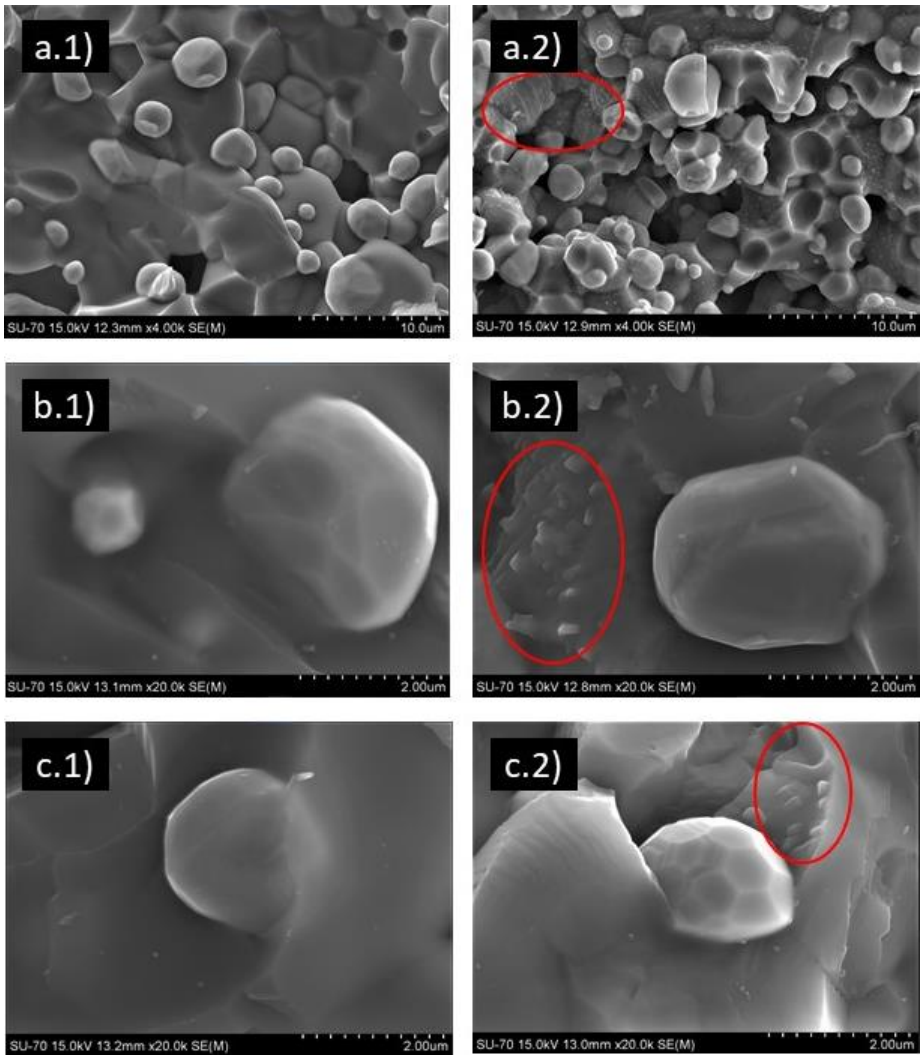


*Figure 3.13. Microstructural analysis of NTO; 0.9NTO and 0.8NTO composition, a, b and c respectively; before and after respectively 1 and 2 by SEM at magnification of 4K for the NTO and 20K for 0.9NTO and 0.8NTO composition.*

## 3.5 Thermodynamic and experimental analysis of the stability issues.

The observed oxidation of Magneli phases at relatively low temperatures during electrical conductivity measurements indicate that they are metastable under these conditions. To analyse this behaviour, an Ellingham diagram with the stability of Magneli phases expressed as equilibrium oxygen partial pressure vs. temperature curves was constructed.

Figure 3.14 represents the thermodynamic data for the various Magneli phases, showing the oxygen partial pressures which correspond to the equilibrium between various Magneli phases. The black line shows the temperature dependence of the actual oxygen partial pressure in the furnace. The crossover of this line with the borderline which corresponds to the formation of Magneli phases takes place only at high temperatures (~1250 ° to 1400 °C), where actually the sintering of the ceramic samples has been done. Therefore, the Magneli phases were formed after this processing step. During relatively fast cooling down after sintering step these phases were retained in the sample in the metastable state. At the temperatures of electrical characterization (right side of the figure 3.14), the stability domain of the Magneli phases corresponds to $p(O_2)$ which is significantly lower than actual oxygen partial pressure in the measurement furnace. This might be a reason for the oxidation of these phases during measurement on heating. Although the oxidation is expected to be partially impeded by slow kinetics at relatively low temperatures, the experimental results indicate that it proceeds quite fast and is accompanied by a significant electrical conductivity drop. It should be noticed that, although the calculated equilibrium stability diagrams (figure 3.14) are quite similar to those presented in [52], the chemical composition of the observed Magneli phases and those predicted from the calculated diagram are slightly different, apparently due to the contribution of the kinetic factor.

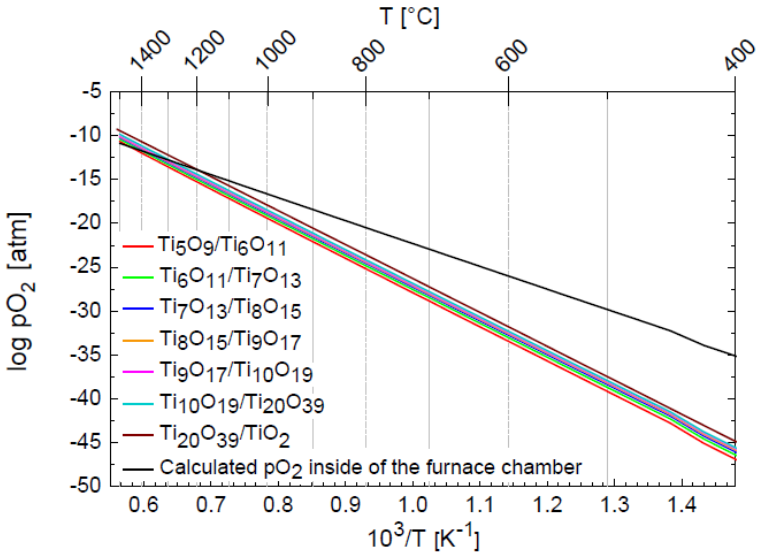


*Figure 3.14. Calculated Ellingham diagram for various Magneli phase pairs.*

Figure 3.15 shows further studies of the stability issues associated with the oxidation of the Magneli phases, by performing in-situ XRD characterization in vacuum with residual pressure of $10^{-3}$ mbar. The studies were carried out for the 0.8NTO composition, which was ground into the

powder to increase the active area for faster reaction, as compared to the bulk ceramic sample used for the conductivity measurements. The oxygen pressure of that atmosphere was $2\times10^{-7}$ atm and was considered independent of temperature, due to the lack of active species as $H_2$ or CO. Up to 550 °C, the phase composition is similar to the initial, further heating to 650 °C results in appearance of the rutile phase. It should be noticed that this temperature is higher than that where noticeable degradation starts for this composition (figure 3.11). During electrical conductivity measurements, the overall duration of the exposure to the intermediate temperature (200-400 °C) range was larger as compared to the XRD. Thus, the oxidation might be kinetically delayed in the case of in-situ XRD characterization. Another possible reason may include the fact that the electrical transport in titanates is extremely sensitive to the oxidation. First stages of the delicate oxidation at relatively low temperatures, like those used for electrical conductivity measurements, could result in the formation of anatase and rutile in partially amorphous state, complicating their detection by XRD, but, at the same time, already suppressing the electrical transport.

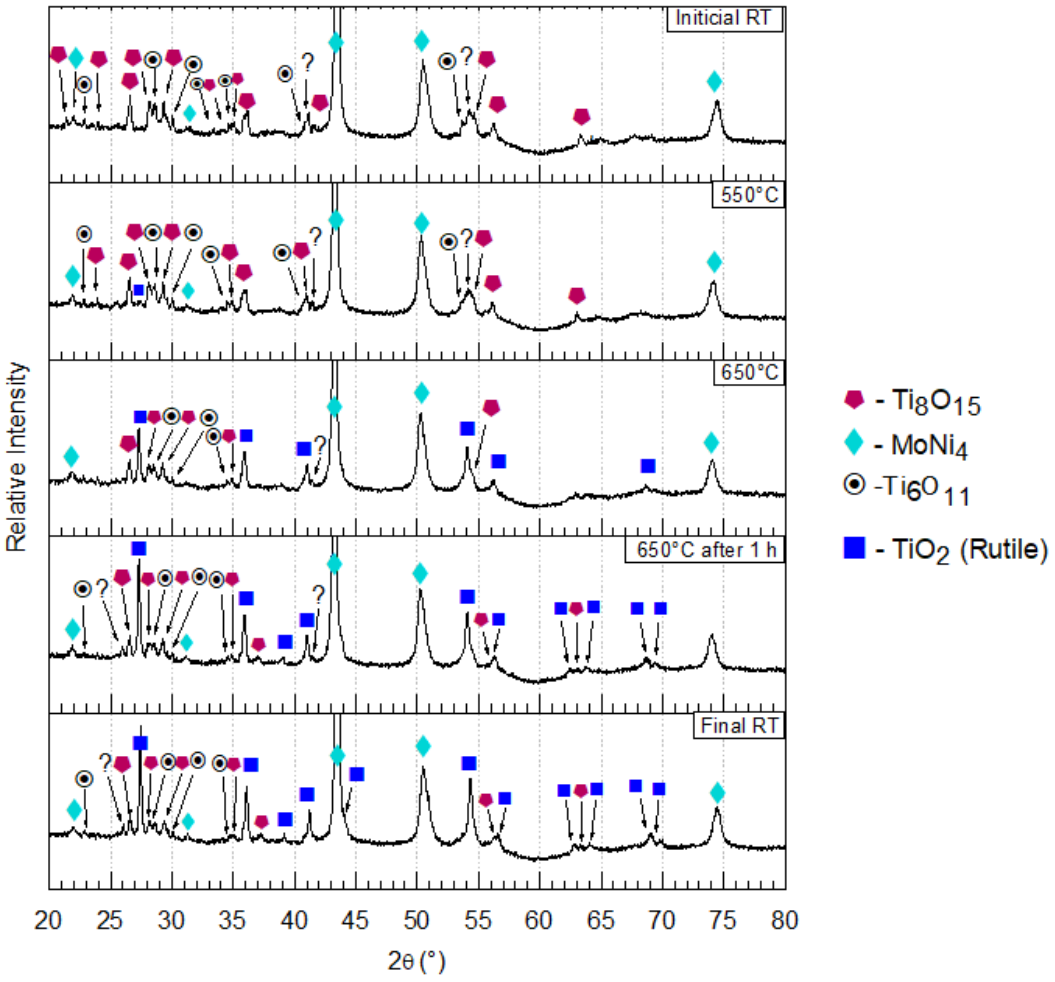


*Figure 3.15. XRD diffraction patterns of NTO80 obtained on heating under vacuum ($p(O_2)= 2\times10^{-7}$ atm).*

The results of additional testing of the phase composition after annealing under 10% $H_2$ + 90% $N_2$ atmosphere at 650 °C for 6 h, performed for the 0.8NTO powder, are shown in figure 3.16.

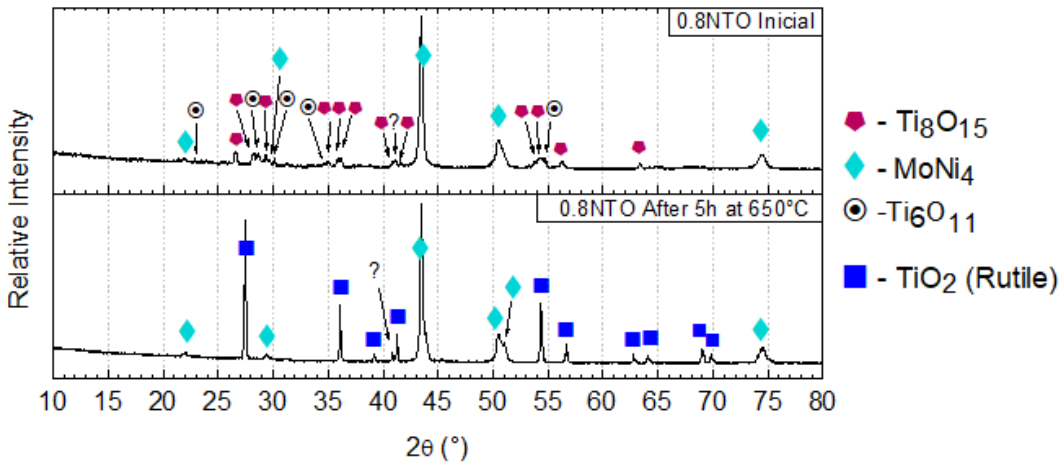


*Figure 3.16. Diffraction patterns of 0.8NTO composition after sintering and annealing at 650 °C during 6 h in 10% $H_2$ + 90% $N_2$ atmosphere.*

Under these conditions, the initial Magneli phases were almost completely transformed to rutile; this may be understood by taking into account the limited redox stability of Magnelli phases in typical $H_2$ - based atmospheres (figure 3.14). Thus, the obtained results suggest that the prepared materials are not suitable as electrodes for reversible SOFC operating even at intermediate temperatures, due to fast degradation of their electrical performance provided by metastability of Magneli phases at these conditions and their tendency to oxidize in nominally inert atmospheres with only traces of oxygen in the ppm range. Nevertheless, the redox gap in figure 3.14 remains relatively small at intermediate temperatures and may be surpassed by cathodic polarization, as predicted by the Nernst equation, for typical conditions at 1073 K, demonstrated by eq. 3.1):

$$\eta_c = \frac{RT}{4F} ln\left(\frac{pO_2^{''}}{pO_2^{'}}\right) \approx \frac{8.314x1073}{4x96500} ln(10^{-3}) = 0.16\,V \qquad \text{eq. 3.1)}$$

In addition, drier atmospheres (i.e. $H_2$:$H_2O$>>1), may also contribute to enhanced redox protection given. Thus, one may still assume potential applicability for operation in steam electrolysis mode.

## 3.6 Electrochemical characterization as potential electrocatalysts for alkaline electrolysis.

Though degradation may compromise prospects for electrochemical applications at intermediate temperatures, sluggish re-oxidation of Magnelli phases may allow prospective applications at lower temperatures, as expected for alkaline electrolysis in aqueous media. In addition, recent literature suggests enhanced electrocatalytic activity of electrodes based on Ni-Mo alloys or intermetallics, and ability to optimize their performance by tuning Mo:Ni ratio and structural features [53], [54].

The figure 3.17 and figure 3.18, are the Pourbaix diagram for 90 °C, of Ni and Mo respectively, those were redrawn, to this temperature, to examine the electrochemical stability of the metallic components of electrocatalysts, during their characterization.

A pure Ni electrode should remain protected in alkaline electrolyte (e.g. pH=14), at the hydrogen evolution potential, whereas cycling from cathodic to anodic polarization may reveal a main oxidation peak above -0.8 V and possibly also above 0.2 V. Other redox changes to still higher oxidation states are likely to appear superimposed on oxygen evolution, possibly affecting their detection.

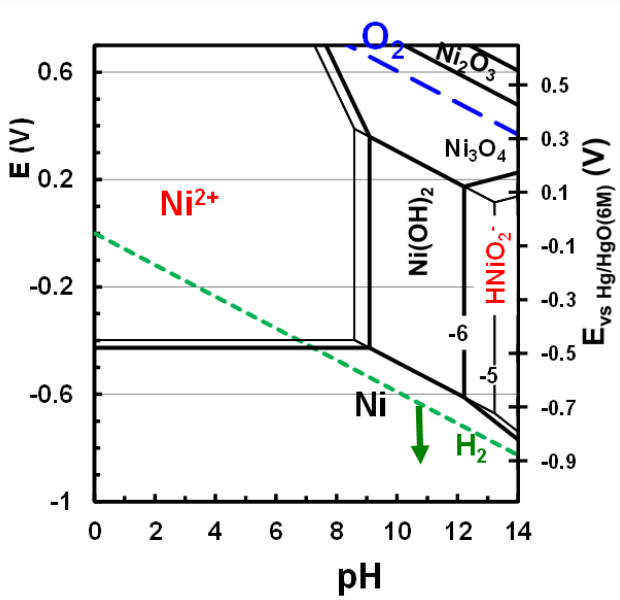


*Figure 3.17. Pourbaix diagram of Ni and related species in aqueous media at room temperature.*

Molybdenum shows poorer stability in alkaline conditions, due to dissolution as ionic species ($MoO_4^{2-}$), and should require significant cathodic polarization below the hydrogen evolution potential, to passivate this metallic electrocatalyst. Nevertheless, these conditions are probably ensured by normal operating conditions of the hydrogen electrode since cathodic protection only requires cathodic polarization of about 0.15 V below the potential of hydrogen evolution (figure 3.18). In addition, stabilization of molybdenum in the $Ni_4Mo$ intermetallic is also expected to hinder its oxidative dissolution.

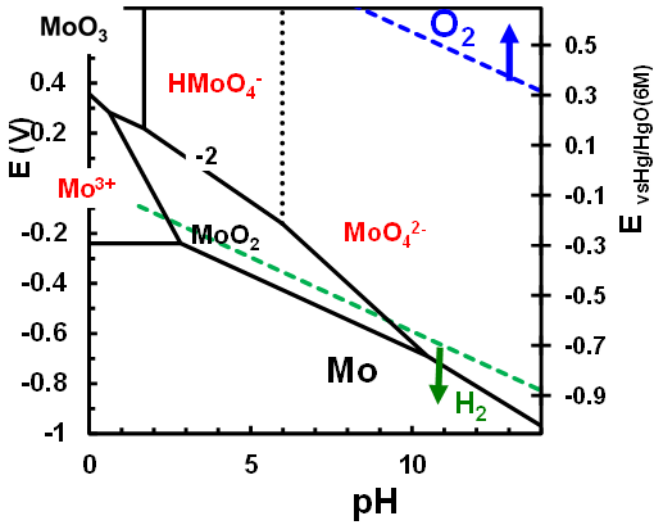


*Figure 3.18. Pourbaix diagram of Mo and related species in aqueous media at room temperature.*

Figure 3.19 is the Ti and Magnelli phases Pourbaix diagram, this one evidences that in an alkaline electrolyte (pH~14), the Magnelli phases show a very narrow stability ranges, except for rutile in anodic conditions and TiO, $Ti_2O_3$ and to lesser extent $Ti_5O_9$, in cathodic conditions in high negative polarization, showing the high stability of rutile in alkaline electrolyte.

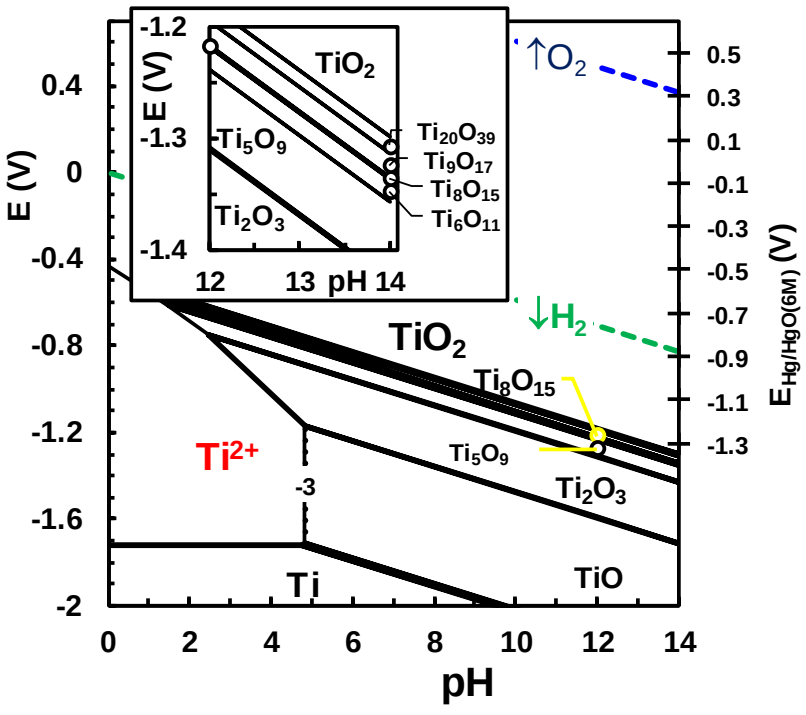


*Figure 3.19. Pourbaix diagram of Ti and its oxides at room temperature, with an expanded area for detailed analysis of electrochemical stability of Magnelli phases.*

One also performed preliminary screening of electrochemistry properties of NTO and Mo-modified materials (0.9NTO and 0.8NTO) in alkaline aqueous media (1M NaOH), by cyclic voltammetry at different scan rates. Results shown in figure 3.20 were obtained at 10 mV/s to detect redox changes of electrode components, with possible impact on the onset of hydrogen and/or oxygen evolution. The Mo-free (NTO) sample shows mainly an oxidation peak (O1) at about -0.7 V vs Hg/HgO/6M NaOH and a reduction peak (R2) at about 0.1 V. By comparison with figure 3.17 one may ascribe O1 to oxidation of metallic Ni to its hydroxide ($Ni(OH)_2$) or the nickelite ion $HNiO_2^-$ , probably displaced to slightly higher potential, for kinetic limitations. R2 is displaced to much higher potential relative to O1 and should be ascribed to transition between a mixed valent state (possibly from $Ni_3O_4$) to the divalent state (possibly $Ni(OH)_2$) as suggested in figure 3.17. Note that cyclic voltammetry fails to show the reducing peak which should correspond to O1, probably because R1 is masked by the prevailing reaction of hydrogen evolution at potential below about -0.9V vs Hg/HgO/6M NaOH.

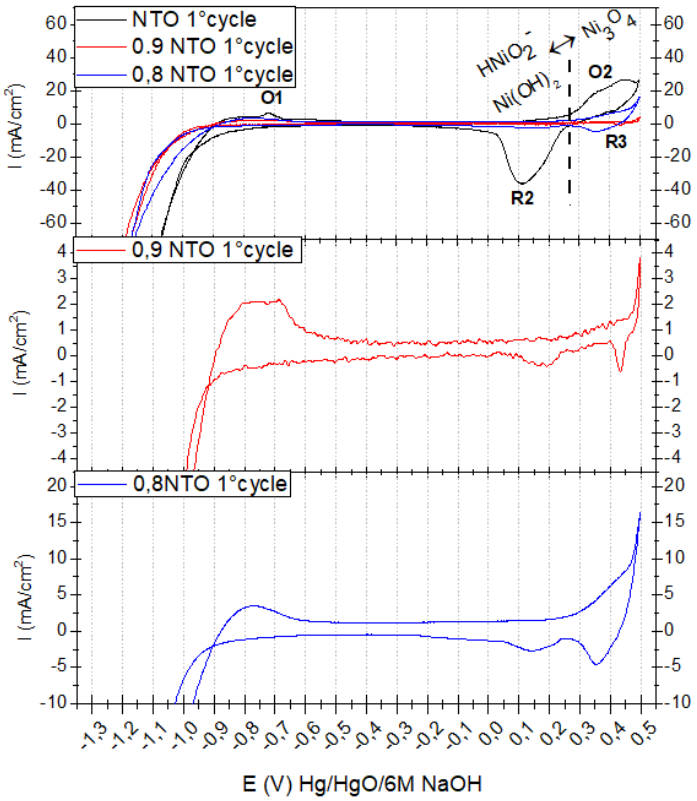


*Figure 3.20. 1 ° cycle of the cyclic voltammetry of electrocatalysts without Mo (NTO), Ni-Mo alloy (0.9NTO) and intermetallic (0.8NTO) in the range -1.3 to 0.5 V vs Hg/HgO (6M), at 10 mV/s as scan rate, and 90 °C.*

In addition, one observes significant hysteresis on cycling above 0.3 V, indicating other redox reactions superimposed on oxygen evolution, namely a second oxidation shoulder (O2) close to 0.35 V and a reduction shoulder at about 0.4 V (R3). Note that shoulders O2 and R3 cannot be ascribed to the same redox reaction since O2 appears at lower potential relative to R3. In addition, R3 is located at a potential in the expected range for reduction of $Ni_2O_3$ to $Ni_3O_4$ (figure 3.17). The corresponding O3 oxidation peak is not shown by cyclic voltammetry possibly because this is well

above the onset of the oxygen evolution above (i.e. >> 0.3 V vs Hg/HgO). The O2 shoulder is likely to correspond to oxidation of $Ni(OH)_2$ to $Ni_3O_4$, which is later reverted by the main R2 reduction peak with decreasing potential.

From the comparison of the different composition, figure 3.20, is noted that the NTO composition presents the highest current intensity when compared with the compositions with Mo. The likely reason for that is the current normalization of the NTO that was overestimated when compared by the other composition, because the area considered for the normalization was the surface area, of the material tested, in contact with the electrolyte. Table 3.6 shown the open porosity in each composition, being noted that the NTO composition presents the highest porosity, due to this one being only uniaxial pressed while the 0.9NTO and 0.8NTO were uniaxial and isostatic pressed. The huge gap of the open porosity shows that the area normalization of the NTO composition, with the other samples was underestimated yielding, maximizing their current intensity.

*Table 3.6. Open porosity of the different composition calculated by Arquímedes' methods.*

| Composition | Open Porosity (%) |
|---|---|
| **NTO** | 48,1 |
| **0,9NTO** | 7,4 |
| **0,8NTO** | 9,5 |

Samples with the $Ni_{0.9}Mo_{0.1}$ alloy (0.9NTO) or intermetallic $Ni_4Mo$ (0.8NTO) do not show any evidence of redox changes for the Mo component. In fact, this would be only expected for potential values well below hydrogen evolution, preventing detection of less intense redox changes. In addition, cyclic voltammetry obtained for samples with Mo additions show clear evidence that the area of R2 of Ni-species is suppressed; this corresponds to lower capacitance, indicating that this redox process is hindered in electrocatalysts based on Ni-Mo alloys or $Ni_4Mo$ intermetallic. The O2 shoulder is also absent or displaced in the cyclic voltammogram of sample 0.9NTO, and somewhat displaced in sample 0.8NTO.

The R3 peak is more obviously observed for sample 0.8NTO, possibly because easy oxidation of Mo may also yield more active Ni by decomposition of the $Ni_4Mo$ intermetallic, contributing to higher oxidation of Ni species. On the contrary, alloying in sample 0.9NTO clearly suppresses the R3 peak and displaces it to higher potential. Thus, it is not obvious if oxidation of the $Ni_{0.9}Mo_{0.1}$ alloy or intermetallic $Ni_4Mo$ may yield a soluble ion $MoO_2^{2-}$, as predicted by the Pourbaix diagram in figure 3.18, or mixed oxide phase such as $NiMoO_4$, which may form in suitable electrochemical [55] or thermochemical conditions [33]. Note also that porosity of the Ni-based sample (NTO) is significantly higher than for samples with Ni-Mo alloy or intermetallic (0.9NTO and 0.8NTO).

Transient behaviour at 0.5 V figure 3.21 and -1.3V figure 3.22 and also emphasize significant differences between samples without and with Mo. At 0.5V vs Hg/HgO/6M NaOH, observes a decay of current density under conditions when Ni may oxidise to the trivalent state figure 3.17) and Mo is likely to oxidise to the hexavalent state (figure 3.18); this suggests passivation by the formation of an oxide or oxy-hydroxide scale. In addition, the very low current density indicates that evolution

of oxygen is also inhibited, contradicting the well known efficiency of Ni anodes in alkaline conditions.

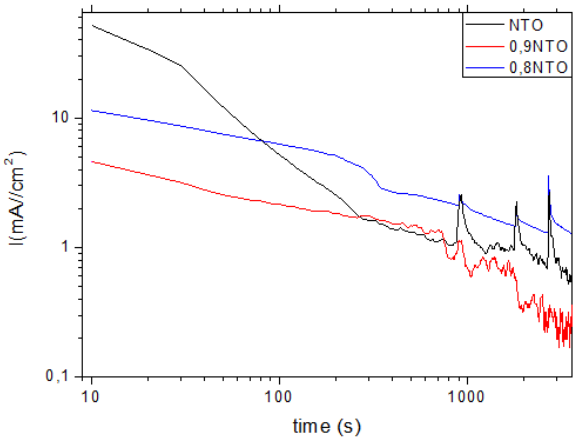


*Figure 3.21. Sequences of 4 steps with 15 min as the duration of transient responses at 0.5 V vs Hg/HgO/6M NaOH.*

While at -1.3 V vs Hg/HgO/6M NaOH observes the major increase in current density, suggesting enhanced hydrogen evolution, mainly for the alloyed sample 0.9NTO. Still, this finding requires further study because results are still away from steady state conditions, and probably affected by previous cycling between anodic and cathodic conditions, inducing corresponding redox changes of Ni and Mo species.

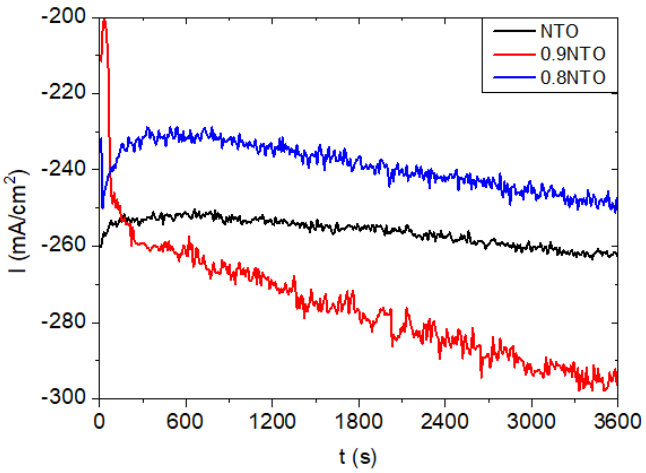


*Figure 3.22. Amperometry with -1.3V as potential during one 1h.*

A plausible cause of this poor performance of NTO, 0.9NTO and 0.8NTO electrocatalysts in conditions of oxygen evolution may be related to dispersion of the Ni-based metallic phase in the oxide matrix formed by titania or related Magnelli phases. Note that the metallic phases appear as isolated grains (figure 3.10), probably below the percolation limit. In section 3.3, this was found to limit applicability in prospective SOFC or SOEC operating condition at intermediate temperatures.

Thus, the actual results indicate that these electrocatalysts are ill suited for oxygen evolution and that performance as hydrogen evolution catalysts may also depend on ability to retain both the Ni-Mo metallic phase and also the conducting ceramic matrix, based on Magnelli phases with required electrical conductivity. One should also consider the ability to regenerate both conducting phases by reverting from anodic polarisation to cathodic polarisation. This was assessed by post-mortem X-Ray analysis (figure 3.23) after a series of cathodic and anodic polarization, with intermediate cyclic voltammetry and electrochemical impedance measurements, namely:

i) Cathodic polarization at -1.3 V vs Hg/HgO/6M NaOH, for 45 min;
ii) Anodic polarization at 0.5 V vs Hg/HgO/6M NaOH, for 60 min;
iii) Cathodic polarization at -1.3 V vs Hg/HgO/6M NaOH for 60 min;
iv) Anodic polarization at 0.5 V vs Hg/HgO/6M NaOH, for 60 min;
v) Cathodic polarization at -1.3 V vs Hg/HgO/6M NaOH for 60 min;

The XRD in figure 3.23 confirms ability to retain Magnelli phases, without evidence for onset of fully oxidised rutile or anatase phases, and also the ability to retain the metallic phase, including the original $Ni_4Mo$ intermetallic in sample 0.8NTO. Indeed, this only refers to bulk phase analysis and may not reveal fine structural changes at the surface scale in contact with the alkaline electrolyte. Nevertheless, the cyclic voltammetry after the anodic polarization steps also reveals relatively fast recovery after those oxidising steps. In fact, complete reduction of both metallic components (Ni and Mo) at -1.3 V is consistent with their Pourbaix diagrams (figure 3.17 and 3.18), whereas the lowest limit of the potential range (-1.3 vs Hg/HgO/6M NaOH) is barely at the electrochemical stability limit of the detected Magnelli phases ( $Ti_8O_{15}$ and $Ti_9O_{17}$), at pH ~14), as shown in figure 3.19. Lower members of the Magnelli series $Ti_nO_{(2n-1)}$ with n≤6) are even less likely to reach cathodic protection with -1.3 V vs Hg/HgO (6M).

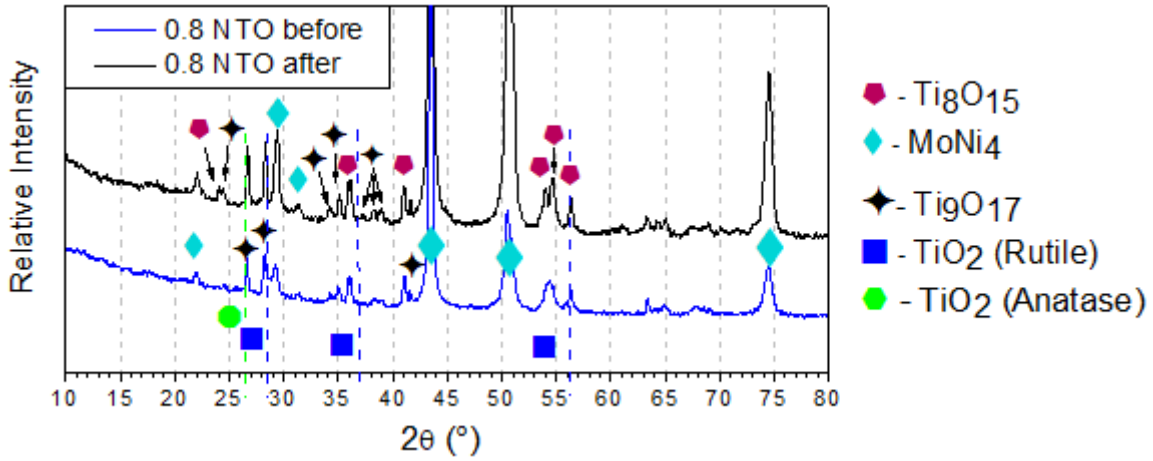


*Figure 3.23. X-Ray diffractograms of 0.8NTO before and after electrochemical testing.*

# 4 Conclusions and future work

In the framework of the proposed thesis, novel (Ni,Mo)-$TiO_2$ composites were assesses as potential electrode materials for several electrochemical applications including reversible solid oxide fuel cells (RSOFC) and alkaline water electrolysis. The intended compositions range corresponded to nominal $NiTiO_3$ (NTO); 90 at% $NiTiO_3$ +10 at% $MoO_3$ (0.9 NTO) and 80 at% $NiTiO_3$ + 20 at% $MoO_3$ (0.8 NTO) precursor powders. The processing approach was based on application of Pechini method, followed by delicate heat treatment to remove the carbon residues and final sintering in air and reducing 10% $H_2$ + 90% $N_2$ atmosphere. The relevant properties of prepared composites were characterized by XRD at different temperatures and atmospheres, SEM/EDS, measurements of electrical conductivity and electrochemical measurements, including cyclic voltammetry and amperometry in alkaline conditions. In addition, thermodynamic predictions of the stability for prepared materials were proposed by calculation of Ellingham and Pourbaix diagrams. The work presents the following main conclusions:

- Preliminary experiments on the powder processing route have shown an importance of careful selection of the burn-out conditions to produce precursor powders with intended oxide composition. Slow heating was required to achieve complete elimination of the carbon residues due to Pechini process without excessive reduction of the nickel species and to maintain maximum homogeneity of the precursor powders. Nickel titanate $NiTiO_3$ represented the major phase in all annealed precursor powders, with additional rutile $TiO_2$ and $NiMoO_4$ phases in the case of Mo-containing materials.

- Attempts to process Mo-containing ceramic samples in air at elevated temperatures (1200 °C) revealed that the major part of molybdenum oxide was evaporated, with only a small fraction possibly incorporated in $NiTiO_3$ structure. These results suggested that the studied materials are rather suitable for the applications where the oxygen partial pressure does not exceed the range from highly-reducing to nearly inert.

- Processing under highly-reducing conditions resulted in the formation of composite material with a matrix based on conductive Magnéli $Ti_nO_{2n-1}$ phase and distributed metallic phases, such as Ni, and presumably $Ni_{0.9}Mo_{0.1}$ alloy and $MoNi_4$ intermetallics in the cases of NTO and Mo-containing compositions, correspondingly, as confirmed by XRD and combined SEM/EDS studies. The composition of Magnéli phases and degree of titanium reduction strongly depended on the porosity of the samples, likely being determined by the diffusion of gaseous reducing species. Thus, relatively fast reduction was observed for 0.9 NTO and 0.8 NTO, where the formation of dense intermetallic compound promotes the porosity, being promising for the electrode applications under reducing environments.

- The electrical measurements have revealed relatively fast degradation of the conductivity even at temperatures of ~400 °C which are below expected range for RSOFC operation. The detailed XRD studies have showed that this degradation is promoted by oxidation of highly-conductive Magnéli phases to insulating rutile phase even under reducing conditions with possible presence of water vapor. The predictions obtained from Ellingham diagrams for various Magnéli phases agree well with the obtained experimental results and confirm that these phases are metastable below 1200 °C under used gas atmosphere. Their formation was

promoted at high sintering temperature, while at lower temperatures they readily oxidize even in nominally inert atmospheres with only traces of oxygen in the ppm range. Thus, the obtained results suggest that the prepared materials are not suitable as electrodes for reversible SOFC operating even at intermediate temperatures.

- Pourbaix diagrams predicted relatively poor stability of Magnéli phases and molybdenum in alkaline conditions, where the formation of ionic $MoO_4^{2-}$ species takes place in a wide range of pH and applied potentials and can be avoided only by significant cathodic polarization below the hydrogen evolution potential. The electrochemical tests in alkaline medium have demonstrated that the prepared materials are not suitable as electrocatalysts for oxygen evolution due to passivation by the formation of an oxide or oxy-hydroxide scale. Their performance as hydrogen evolution catalysts depends on the ability to retain highly-conductive Magnéli phases in the matrix and to avoid the decomposition of Ni-Mo metallic phase. In the case of excessive oxidation, cathodic polarization is effective for at least partial recovery of the conducting phases, in accordance with the predictions from Pourbaix diagrams.

Future work on similar materials as electrodes for RSOFC or AWE applications may include:

- Percolation improvement of the metallic particles by increasing their amount or by sintering in lower temperature to impede the grain growth. This is expected to reduce the negative effects produced by oxidation of the Magneli phases and corresponding electrical conductivity degradation.
- Since the prepared materials appear to be at least partially suitable as electrodes for hydrogen evolution in AWE applications, the characterization must be extended to higher time scales for the cathodic and anodic polarization, in order to obtain additional guidelines for seeking conditions for stable performance and fast recovery by redox cycling. To understand deeper the surface electrode mechanisms, additional post-mortem X-ray photoelectron spectroscopy (XPS) studies would be useful.

# Bibliografia


[1] M. Little, M. Thomson e D. Infield, “Electrical integration of renewable energy into stand-alone power supplies incorporating hydrogen storage,” *International Journal of Hydrogen Energy ,* vol. 32, pp. 1582-1588, 2007.

[2] S. B. T. A. “. 1. E. c. 3. Christophe Coutanceau, em *Hydrogen Electrochemcial Production*, Academic Press, 2017, pp. 17-62.

[3] F. M. Sapountzi, J. M. Gracia, C. J. Weststrate, H. O. A. Fredriksson e J. W. Niemantsverdriet, “Electrocatalysts for the generation of hydrogen, oxygen and synthesis gas,” *Progress in Energy and Combustion Science,* vol. 58, pp. 1-35, 2017.

[4] M. A. L. Bercero, “Recent advances in high temperature electrolysis using solid oxide fuel cells: A review,” *Journal of Power Sources,* vol. 203, pp. 4-16, 2012.

[5] M. Carmo, D. L. Fritz, J. Mergel e D. Stolten, “A comprehensive review on PEM water electrolysis - Review,” *Internacional Journal of Hydrogen Energy,* vol. 38, pp. 4901-4034, 2013.

[6] S. Mekhilef, R. Saidur e A. Safari, “Comparative study of different fuel cell technologies,” *Renewable and Sustainable Energy Reviews,* vol. 16, pp. 981-989, 2012.

[7] K. Zeng e D. Zhang, “Recent progress in alkaline water electrolysis for hydrogen production and applications,” *Progress in Energy and Combustion Science,* vol. 36, pp. 307-326, 2010.

[8] S. Marini, P. Salvi, P. Nelli, R. Pesenti, M. Villa, M. Berrettoni, G. Zangari e Y. Kiros, “Advanced alkaline water electrolysis,” *Electrochimica Acta,* vol. 82, pp. 384-391, 2012.

[9] C. P. K. M. Xiang e N. S. Lewis, “Principles and implementations of electrolysis systems for water splitting,” *The Royal Society of Chemistry: Mater. Horiz.,* vol. 3, pp. 169-173, 2016.

[10] F. Safizadeh, E. Ghali e G. Houlachi, “Electrocatalysis developments for hydrogen evolution reaction in alkaline solutions – A review,” *International Journal of Hydrogen Energy,* vol. 40, pp. 256-274, 2015.

[11] L. Birry e A. Lasia, “Studies of the hydrogen evolution reaction on Raney nickel-molybdenum electrodes,” *Journal of Applied Electrochemistry,* vol. 34 , pp. 735-749, 2004.

[12] X. Tang, L. Xiao, C. Yang, J. Lu e L. Zhuang, “Noble fabrication of Ni-Mo cathode for alkaline water electrolysis and alkaline polymer electrolyte water electrolysis,” *International Journal of Hydrogen Energy ,* vol. 39, pp. 3055-3060, 2014.

[13] A. J. Esswein, M. J. McMurdo, P. N. Ross, A. T. Bell e T. D. Tilley, “Size-Dependent Activity of Co3O4 Nanoparticle Anodes for Alkaline Water Electrolysis,” *The Journal of Physical Chemistry C,* vol. 113, pp. 15068-15072, 2009.

[14] G. Schiller, R. Henne e P. a. P. V. Mohr, “High performance electrodes forn an advanced intermittently operated 10kW alkaline water electrolyzer,” *International Journal of Hydrogen Energy ,* vol. 23, pp. 761-765, 1998.

[15] H. Michishita, Y. Misumi, D. Haruta, T. Y. N. Masaki e H. I. T. Matsumoto, “Cathodic Performance of La0.6Sr0.4 CoO3 Perovskite Oxide for Platinum-Free Alkaline Water Electrolysis cell,” *Journal of the Electrochemical Society,* vol. 155, n ° 9, pp. B969-B971, 2008.

[16] S. Y. Gómez e D. Hotza, “Current developments in reversible solid oxide fuel cells,” *Renewable and Sustainable Energy Reviews,* vol. 61, pp. 155-174, 2016.

[17] K. Eguchi, T. Hatagishi e H. Arai, “Power generation and steam electrolysis characteristics of an electrochemical cell with a zirconia- or ceria-based electrolyte,” *Solid State Ionics,* Vols. %1 de %286-88, pp. 1245-1249 , 1996.

[18] F. Tietz, D. Sebold, A. Brisse e J. Schefold, “Degradation phenomena in a solid oxide electrolysis cell after 9000 h of operation,” *Journal of Power Sources,* vol. 223, pp. 129-135, 2013.

[19] J. Kim, H. Ji, H. Dasari, D. Shin, H. Song, J. H. Lee, B. K. Kim, H. J. Je, H. W. Lee e K. J. Yoon, “Degradation mechanism of electrolyte and air electrode in solid oxide electrolysis cells operating at high polarization,” *International Journal of Hydrogen Energy ,* vol. 38, n ° 3, pp. 1225-1235, 2013.

[20] M. A. Laguna-Bercero, H. Monzon, A. Larrea e V. M. Orera, “Improved stability of reversible solid oxide cells with a nickelate-based oxygen electrode,” *Journal of Materials Chemistry A,* vol. 4, pp. 1446-1453, 2016.

[21] D. Waldbillig, A. Wood e D. G. Ivey, “Electrochemical and microstructural characterization of the redox tolerance of solid oxide fuel cell anodes,” *Journal of Power Sources,* vol. 145, n ° 2, pp. 206-215, 2005.

[22] D. Sarantaridis e A. Atkinson, “Redox cycling of Ni-based Solid Oxide Fuel Cell Anodes: A review,” *Fuel Cells,* vol. 7, n ° 3, pp. 246-258, 2007.

[23] Y. H. Heo, J. W. Lee, S. B. Lee, T. H. Lim, S. J. Park, R. H. Song, C. O. Park e D. R. Shin, “Redox-induced performance degradation of anode-supported tubular solid oxide fuel cells,” *International Journal of Hydrogen Energy,* vol. 36, n ° 1, pp. 797-804, 2011.

[24] M. Ettler, H. Timmermann, J. Malzbender, A. Weber e N. H. Menzler, “Durability of Ni anodes during reoxidation cycles,” *Journal of Power Sources ,* vol. 195, n ° 17, pp. 5452-5467, 2010.

[25] Q. Bkour, K. Zhao, L. Scudiero, D. J. Han, C. W. Yoon, O. G. Marin-Flores, M. G. Norton e S. Ha, “Synthesis and performance of ceria-zirconia supported Ni-Mo nanoparticles for partial oxidation of isooctane,” *Applied Catalysis B: Environmental,* vol. 212, p. 97–105, 2017.

[26] Z. Wang, Z. Wang, W. Yang, R. Peng e Y. Lu, “Carbon-tolerant solid oxide fuel cells using NiTiO3 as an anode internal reforming layer,” *Journal of Power Sources,* vol. 255, pp. 404-409, 2014.

[27] S. Bagheri, N. M. Julkapli e S. B. A. Hamid, “Titanium Dioxide as a Catalyst Support in Heterogeneous Catalysis,” *The Scientific World Journal,* 2014.

[28] P. Tiwari e S. Basu, “Ni infiltrated YSZ anode stabilization by inducing strong metal support interaction between nickel and titania in solid oxide fuel cell under accelerated testing,” *International Journal of Hydrogen Energy,* vol. 38, n ° 22, pp. 9494-9499, 2013.

[29] H. Ellingham, “Transactions and Communications,” *Journal of the Society of Chemical Industry (London),* vol. 63, p. 125, 1944.

[30] L. M. Madeira, M. F. Portela e C. Mazzocchia, “Nickel Molybdate Catalysts and Their Use in the Selective Oxidation of Hydrocarbons,” *Catalysis Review: Science and Engineering,* vol. 46, pp. 53-110, 2004.

[31] X. Hou, K. Zhao, O. A. Marina, M. G. Norton e S. Ha, “NiMo-ceria-zirconia-based anode for solid oxide fuel cells operating on gasoline surrogate,” *Applied Catalysis B: Environmental,* vol. 242 , pp. 31-39, 2019.

[32] K. Zhao, X. Hou, Q. Bkour, M. G. Norton e Ha, “NiMo-ceria-zirconia catalytic reforming layer for solid oxide fuel cells running on a gasoline surrogate,” *Applied Catalysis B: Environmental,* vol. 224, pp. 500-507, 2018.

[33] K. T. Jacob, G. Kale e G. Iyengar, “Phase equilibria and thermodynamic properties in the system Ni-Mo-O,” vol. 22, n ° 12, pp. 4274-4280, 1987.

[34] T. Massalski, J. L. Murray e L. H. B. H. Bennett, Binary alloy phase diagrams, vol. 2, American Society for Metals, 1986, p. 1610.

[35] C. Mazzocchia, C. Aboumrad, C. Diagne, E. Tempesti, J. Herrmann e G. Thomas, “On the NiMoO4 oxidative dehydrogenation of propane to propene: some physical correlations with the catalytic activity,” *Catalysis Letters,* vol. 10, pp. 181-192, 1991.

[36] D. C. Coelho, A. C. Oliveira, J. M. Filho, A. C. Oliveira, A. F. Lucredio, E. M. Assad e E. Rodríguez-Castellón, “Effect of the active metal on the catalytic activity of the titanate nanotubes for dry reforming of methane,” *Chemical Engineering Journal,* vol. 290, pp. 438-453, 2016.

[37] K. Li, L. W. X. P. J. Jia, B. Chi e J. Li, “Enhanced methane steam reforming activity and electrochemical performance of Ni0.9Fe0.1-supported solid oxide fuel cells with infiltrated Ni-TiO2 particles,” *Scientific Reports,* vol. 6, p. 35981, 2016.

[38] K. T. Jacob, V. S. Saji e S. Reddy, “Thermodynamic evidence for order-disorder transition in NiTiO3,” *The Journal of Chemical Thermodynamics,* vol. 39, n ° 2, pp. 230-235, 2007.

[39] H. Sekimoto, T. Uda, Y. Nose e S. Sato, “Reduction of titanium oxide in the presence of nickel by nonequilibrium hydrogen gas,” *Journal of Materials Research,* vol. 24, n ° 7, pp. 2391-2399, 2009.

[40] L. Glasser, “Systematic Thermodynamics of Magnéli-phase and Other Transition Metal Oxides,” *Inorganic Chemistry,* vol. 48, pp. 10289-10294, 2009.

[41] C. Z. S. Shi, X. Z. A. Li, M. Shi, Y. Zhu, J. Qiu e C. Au, “Synergism in NiMoOx precursors essential for CH4/CO2 dry reforming,” *Catalysis Today,* vol. 233, pp. 46-52, 2014.

[42] A. Kovalevsky, A. Yaremchenko, S. Populoh, A. Weidenkaff e J. Frade, “Enhancement of thermoelectric performance in strontium titanate by praseodymium substitution,” *Journal of Applied Physics,* vol. 113, p. 053704, 2013.

[43] G. Eriksson e A. D. Pelton, “Metallurgical Transactions B,” *Critical evaluation and optimization of the thermodynamic properties and phase diagrams of the MnO-TiO2, MgO-TiO2, FeO-TiO2, Ti2O3-TiO2, Na2O-TiO2, and K2O-TiO2 systems,* vol. 24, pp. 795-805, 1993.

[44] D. V. Lopes, Y. A. Ivanova, A. V. Kovalevsky, A. R. Sarabando, J. R. Frade e M. J. Quina, “Electrochemical reduction of hematite-based ceramics in alkaline medium: challenges in electrode design,” *Electrochimica Acta ,* vol. 327, n ° 135060, 2019.

[45] M. Pourbaix, Atlas of Electrochemical Equilibria in Aqueous Solutions, 2 ed., Nace International,, 1974.

[46] Y. A. Ivanova, J. Monteiro, L. Teixeira, N. Vitorino, A. Kovalevskya e J. Frade, “Designed porous microstructures for electrochemical reduction of bulk hematite ceramics,” *Materials & Design,* n ° 122, pp. 307-314, 2017.

[47] G. R. Belton e A. S. Jordan, “The volatilization of the Molybdenum in the presence of water vapor,” *The Journal of Physical Chemistry,* vol. 6, n ° 69, pp. 2065-2071, 1965.

[48] N. Floquet, O. Bertrand e J. J. Heizmann, “Structural and Morphological Studies of the Growth of MoO3 Scales During High- Temperature Oxidation of Molybdenum,” *Oxidation of metals,* n ° 37, pp. 253-280, 1992.

[49] J. Zhang, T. Wang, P. Liu, Z. Liao, S. Liu, X. Zhuang, C. Mingwei, E. Zschech e X. (. 8. Feng, “Efficient hydrogen production on MoNi4 electrocatalysts with fast water dissociation kinetics,” *Nature Communications ,* n ° 8, p. 15437, 2017.

[50] M. H. Pihlatie, A. Kaiser, M. Mogensen e C. M., “Electrical conductivity of Ni-YSZ composites: Degradation due to Ni particle growth,” *Solid State Ionics,* n ° 189, pp. 82-90, 2011.

[51] F. C. Walsh e R. G. A. Wills, “The continuing development of Magnéli phase titanium sub-oxides and Ebonex® electrodes,” *Electrochimica Acta,* n ° 55, pp. 6342-6351, 2010.

[52] Y. B. Kang e H. Lee, “Experimental Study of Phase Equilibria in the MnO-“TiO2”-“Ti2O3” System,” *ISIJ International,* vol. 45, n ° 11, pp. 1543-1551, 2005.

[53] G. Cao, Z. Chen, H. Yin, L. Gan, M. Zang, N. Xu e P. Wang, “Investigation of the correlation between the phase structure and activity of Ni–Mo–O derived electrocatalysts for the hydrogen evolution reaction,” *Journal of Materials Chemistry A,* n ° 7, p. 10338, 2019.

[54] X. Zheng, Y. He, J. Chen, D. Gao, Y. Zhang, P. Xiao e W. Tian, “NimMon (m + n = 5) Clusters for Hydrogen Electric Reduction: Synergistic Effect of Ni and Mo on the Adsorption and OH Breaking of H2O,” *The Journal of Physical Chemistry C,* vol. 14, n ° 123, pp. 9247-9254, 2019 .

[55] V. Kumbhar, V. Nguyen, Y. Lee, C. Lokhande, D. Kim e J. Shim, “Electrochemically growth-controlled honeycomb-like NiMoO4 nanoporous network on nickel foam and its applications in all-solid-state asymmetric supercapacitors,” *New Journal of Chemistry,* n ° 42, p. 14805, 2018.